NASA-TM - 58266

NASA Technical Memorandum 58266

NASA-TM-58266 19850016900

A Three-Dimensional Navier-Stokes/Euler Code for Blunt-Body Flow Computations

Chien-peng Li

[illegible]

April 1985

LIBRARY COPY

MAY 2[illegible] 1985

LANGLEY RESEARCH CENTER
LIBRARY, NASA
HAMPTON, VIRGINIA

National Aeronautics and
Space Administration

Lyndon B. Johnson Space Center
Houston, Texas

NASA Technical Memorandum 58266

A Three-Dimensional Navier-Stokes/Euler Code for Blunt-Body Flow Computations

Chien-peng Li
Lyndon B. Johnson Space Center
Houston, Texas

N A S A
National Aeronautics and
Space Administration

Scientific and Technical
Information Branch

1985

N85-25211#

```
ENTER:
 14      1      1 RN/NASA-TM-58266
           DISPLAY 14/2/1
      85N25211*#   ISSUE 15   PAGE 2463   CATEGORY 2   RPT#: NASA-TM-58266 S-546
      NAS 1.15:58266   85/04/00  27 PAGES   UNCLASSIFIED DOCUMENT
UTTL: A 3-dimensional Navier-Stokes-Euler code for blunt-body flow computations
AUTH: A/LI, C. P.
CORP: National Aeronautics and Space Administration. Johnson (Lyndon B.) Space
      Center.     AVAIL.NTIS   SAP: HC A03/MF A01
MAJS: /*BLUNT BODIES/*EULER EQUATIONS OF MOTION/*FLOW DISTRIBUTION/*HYPERSONIC
      FLOW/*NAVIER-STOKES EQUATION
MINS: / COMPUTATIONAL FLUID DYNAMICS/ FINITE DIFFERENCE THEORY/ NUMERICAL
      ANALYSIS/ WIND TUNNEL TESTS
ABA:  E.A.K.
ABS:  The shock-layer flowfield is obtained with or without viscous and
      heat-conducting dissipations from the conservative laws of fluid dynamics
      equations using a shock-fitting implicity finite-difference technique. The
      governing equations are cast in curvilinear-orthogonal coordinates and
      transformed to the domain between the shock and the body. Another set of
      equations is used for the singular coordinate axis, which, together with a
      cone generator away from the stagnation point, encloses the computation
      domain. A time-dependent alternating direction implicit factorization
      technique is applied to integrate the equations with local-time increment
      until a steady solution is reached. The shock location is updated after
      the flowfield computation, but the wall conditions are implemented into
ENTER:
           DISPLAY 14/2/1
      the implicit procedure. Innovative procedures are introduced to define the
      initial flowfield, to treat both perfect and equilibrium gases, to advance
      the solution on a coarse-to-fine grid sequence, and to start viscous flow
      computations from their corresponding inviscid solutions. The results are
      obtained from a grid no greater than 28 by 18 by 7 and converged within
      300 integration steps. They are of sufficient accuracy to start
      parabolized Navier-Stokes or Euler calculations beyond the nose region, to
      compare with flight and wind-tunnel data, and to evaluate conceptual
      designs of reentry spacecraft.
```

CONTENTS

Section Page

Abstract 1

1 Introduction 1

2 Theoretical Formulation 2
2.1 Geometric Consideration and Coordinate Systems 2
2.2 Equations in Computation Space 3
2.3 Mapping Functions 4
2.4 Boundary Conditions 4
2.5 Initial Flow Approximation 5
2.6 Wall Shear, Heat Flux, and *L/D* Calculations 6

3 Implicit Difference Method 6
3.1 Difference Approximations 6
3.2 ADI Factorization Technique 7
3.3 Jacobian Matrices 8
3.4 Numerical Damping and Time Increment 9

4 Code Capabilities and Limitations 9

5 Discussion of Sample Cases 10

Concluding Remarks 12

References 12

Appendix A - Derivation of Eq. (2) 13

TABLES

Table Page

1 Unit vectors in reference coordinate frames 14

2 List of sample cases 14

FIGURES

Figure Page

1 Capabilities of the Navier-Stokes/Euler blunt-body code

a) Portion of a complete Orbiter flowfield 15
b) Stagnation region of blunt body 15
c) OTV with raked-off body 15

2 Schematic of the physical and computational coordinates . . 15

3 Comparison of the grid-clustering functions 15

4 Convergence history for 2D NSWC-1 case

a) Effects of time-increment step size on inviscid solution 16
b) Effects of local-time integration on inviscid solution 16
c) Comparison between global- and local-time convergence rates for viscous case 16

5 Inviscid flowfield results for the NSWC-1 case (M = 2.97, α = 0°); X_{max} = 0.58102. Shock speed: 0.003187 (left plot); 0.005339 (right plot) 17

6 Comparison of NS and BL results for an AEDC 2D case

a) Wall pressure distribution 17
b) Friction coefficient 17
c) Heat-transfer coefficient 17

7 Convergence history for an AEDC 3D case and effects of damping parameters 18

8 Comparison of friction and heat-transfer coefficients for an AEDC 3D case using different time-step sizes 18

9 Inviscid flowfield results for the NSWC-2 case (M = 5.94, α = 10°); X_{max} = 0.9496. Shock speed, 0.017368 (left plot); stagnation pressure, 44.5016 (right plot) 18

10 Viscous flowfield results for the NSWC-2 case (M = 5.94, α = 10°); X_{max} = 0.9496. Stagnation Stanton number, 0.00374 (left plot); stagnation pressure, 43.2118 (right plot) 19

11 Inviscid flowfield results for the AEDC case (M = 8, α = 30°). X_{max} = 1.2161; stagnation pressure, 77.2282 19

Figure Page

12 Viscous flowfield results for the AEDC case (M = 8, α = 30°). X_{max} = 1.2161; stagnation pressure, 82.1822 (right plot); stagnation Stanton number, 0.03695 (left plot) . . 19

13 Inviscid and viscous flowfield results for the Orbiter case (M = 22, α = 40.8°, equilibrium air); X_{max} = 1.613. Stagnation Stanton number, 0.03796 (left plot); stagnation pressure, 663.748 (right plot) 19

14 Shock shape and comparison with flight data for the Orbiter case (α = 40.8°, t = 650 sec). X_{max} = 1.613; stagnation Stanton number, 0.040736 20

15 Shock shape for the OTV case (M = 34.8, α_T = 15°) 20

16 Inviscid and viscous flowfield results for the OTV case; X_{max} = 2.493. Stagnation Stanton number, 0.02512 (lower right); stagnation pressure: 1540.56 (upper left); 1553.33 (lower left, viscous case) 20

Abstract

The shock-layer flowfield is obtained with or without viscous and heat-conducting dissipations from the conservative laws of fluid dynamics equations using a shock-fitting implicit finite-difference technique. The governing equations are cast in curvilinear-orthogonal coordinates and transformed to the domain between the shock and the body. Another set of equations is used for the singular coordinate axis, which, together with a cone generator away from the stagnation point, encloses the computation domain. After initializing the flow variables on a prescribed grid, a time-dependent alternating direction implicit factorization technique is applied to integrate the equations with local-time increment until a steady solution is reached. The shock location is updated after the flowfield computation, but the wall conditions are implemented into the implicit procedure. Since primitive variables and few metrics are used, the numerical formulation is simple and the core requirement is not stringent. Innovative procedures have been introduced to define the initial flowfield, to treat both perfect and equilibrium gases, to advance the solution on a coarse-to-fine grid sequence, and to start viscous flow computations from their corresponding inviscid solutions. The code has proven capabilities for a wide range of free-stream conditions and body configurations. Among the examples shown are the Space Shuttle Orbiter equilibrium flow case at Mach 22 and an angle of attack of 40.8°, and an aerobraking orbital transfer vehicle perfect-gas case having a 60° cone and sonic shoulder at Mach 34.8. These results are obtained from a grid no greater than 28 by 18 by 7 and converged within 300 integration steps. They are of sufficient accuracy to start parabolized Navier-Stokes or Euler calculations beyond the nose region, to compare with flight and wind-tunnel data, and to evaluate conceptual designs of reentry spacecraft.

1. Introduction

Although the solutions of blunt-body flow have been pursued ever since the beginning of supersonic flight, they received most attention later in the design of spacecraft to alleviate the aerodynamic heating during entry. If the viscous effect is confined to a thin boundary layer adjacent to the body, the inviscid assumption can be invoked to simplify the complexity of the problem. Even so, the governing equations are nonlinear and of mixed characteristics bounded by the bow shock; hence, only numerical methods are applicable. The classical approaches for inviscid flow computation developed before 1960 have been summarized in the book by Hayes and Probstein,(1) wherein three-dimensional (3D) problems were barely touched because of the limited computer resources available then. The new era of blunt-body flow computation began with the pioneering work of Moretti,(2) who introduced a shock-fitting procedure to the well-formulated time-dependent finite-difference approach. The problem has become a time-dependent, or iterative, solution starting from a reasonable guess of shock location and shock-layer variables, whereby a firm theory of initial-value problems can be used. Moretti and Bleich's(2) three-dimensional code was made available in 1967. Since then, it was improved and adopted by many organizations for their specific applications. The most important ones, probably, are the finite-volume code by Rizzi and Inouye,(3) the λ-scheme code by Hall,(4) and the split-coefficient code by Daywitt.(5) Whereas smooth bodies are the objective aimed at in Refs. 2 and 3, indented nosetips are of primary interest as investigated in Refs. 4 and 5. These Euler codes are based on explicit technique and confined to the shock layer, a common feature shared by many other versions developed in the 1970 decade.

The development of three-dimensional Navier-Stokes (3D NS) codes has progressed relatively slowly but still shown impressive accomplishment. The first attempt was made by the author(6) in 1974, when he used MacCormack's two-step scheme and a finite-difference procedure to calculate the shock and body variables as opposed to using Moretti's characteristic procedure. Since dense grid points used to resolve the diffusive fluxes near the wall penalized the rate of convergence, results were unsatisfactory even at the cost of several hundred hours of IBM 360-67 computer time.(7) Obviously, after demonstrating the feasibility of NS methodology, more powerful numerical techniques and computers are needed to perform any computation for practical purposes. As soon as Beam and Warming's alternating direction implicit (ADI) factorization technique(8) became fully developed, it was adapted and modified to be suitable for the peculiarity of blunt-body problems. The computation time was reduced to a mere 10 hr of Univac 1182 computer because of the use of less restricted time-step size. The implicit code was used successfully to solve some very difficult problems for the Space Shuttle Orbiter at high angles of attack, and preliminary results have been reported in 1981.(9) During this period, Kutler et al.(10) developed a 3D shock-fitting NS code on the basis of Pulliam and Steger's(11) generalized-coordinate NS code. Since the motivation of Kutler's work came from the need to predict aerodynamic characteristics for an indented nosetip at relatively low angles of attack, the code is known to have had stability difficulties and failed to converge for flow incidence angles of greater than 30°.

The purpose of this paper is to present the detailed formulation, the method of computation, and the verification sample cases of the 3D NS code, which has undergone continued refinement since 1981. A substantial acceleration of convergence rate has been realized by means of implicit damping and of local-time step at a constant Courant number (CN). The accuracy of equilibrium-air solution is enhanced by using Tannehill's routines for the equation of state and the transport coefficients.(12,13) Additional schemes to sequence the computations from coarse to fine grids are also found useful to shorten the number of iteration cycles. The performance of the 3D NS code is much superior to that of its original version, the capabilities of considering different body geometries have been broadened, and strong flow asymmetry can be easily handled.

The code is intended to meet two main requirements: prediction of wall heat-flux distribution and definition of flow variables on an axial plane in the supersonic region. The NS methodology is applicable to blunt reentry spacecraft at high altitude where the low-density and low-Reynolds-number conditions invalidate the thin boundary-layer (BL) assumption for a decoupled Euler and BL approach. The NS code is also needed for determining the flowfield around a highly blunt body truncated by a sonic shoulder as the pressure and boundary layer are strongly influenced by the abrupt change of body contour. Generation of flow variables to start the downstream computation by a space-marching technique can be conventionally done with an axisymmetric two-dimensional (2D) code for a spherical nose. However, for nonspherical nose shapes and high angles of attack, the 3D NS code should be used.

The formulation and methods of calculation are tailored to satisfy the goals and selected for use on scalar computers (Univac 1182) having 3 million instructions per second (MIPS) and 262 000 words of main core. In view of the body configurations illustrated in Fig. 1 and the absence of embedded shocks, the conventional, weakly conservative NS equations are cast in curvilinear-orthogonal coordinates and converted to the spherical-polar frame by two metrics. The singular axis is governed by a different set of NS equations in order to eliminate solution errors introduced by other means of solution. A straightforward central-difference quotient is used to approximate the derivatives of the convective and diffusive flux terms. The numerical solution is time-dependent starting from an approximate shock and initial assumption of flow variables. The shock is fitted explicitly, but the wall and the shock layer itself are updated by the ADI factorization technique, which, in turn, leads to three systems of linear algebraic equations of block-matrix structure. Primitive variables are sought for by the implicit solution to lessen the amount of arithmetic in evaluating Jacobians. The Euler solution is often obtained to initialize the NS computation, although, in some cases, the direct application of coarse-to-fine grid sequence is more cost-effective for NS computations. Either is needed to reduce the computation cost.

The remaining portion of the paper is divided into four sections and an appendix. The vector notation of coordinate systems is defined immediately following this section. Duplication of governing equations already presented in earlier publications(6,9) cannot be totally avoided for the completeness of this final report. In the third section, the well-known factorization technique is briefly outlined with emphasis placed on the Jacobian matrices and damping terms which are different from other work.(8,10,11) The fourth section is intended to summarize the capabilities and limitations of the 3D NS code and includes remarks on proper use of the code. The discussion of results in sec. 5 begins with the explanation of important parameters and their effects on the solution, then ends with sample results demonstrating the code usage. Appendix A contains detailed derivation of the governing equations on the singular coordinate axis.

2. Theoretical Formulation

2.1 Geometric Consideration and Coordinate Systems

Because of the commonness of blunt entry bodies, a flowfield solution is often needed to provide the heat-flux distributions over a nonspherical nose, wide-angle body with sonic shoulder and to determine the flow variables on an axial plane for computations downstream. Figure 1 depicts the three basic configurations differing in the orientation of the coordinate system and the wind direction. The flow incidence angle α and the reference angle α_T have either a positive value or a zero as shown, or both can have positive values for additional convenience to define the region of interest. For most cases, there is a plane of symmetry so that the flowfield is only needed to the right side of the wind vector. The computation region extended from the body to the shock and enclosed by the Z-axis, and the cone generator with various vertex angles are seen in Fig. 1. As has been done in practice, a spherical-polar system is used to define the physical space over the frontal portion of the blunt body, then a cylindrical-polar system is used downstream of the interface shared by both coordinate systems.(6,9) If a more complicated body such as an indented nose is to be considered, conformal mappings of meridional plane may be used to generate a family of coordinate lines less oblique to the body wall than those in the spherical system. Fortunately, the lack of control of the location and the orientation of the coordinate lines at the boundary does not pose a serious limitation to the computation of smooth bodies. Furthermore, the present formulation requires only two metrics in contrast to nine metrics and a Jacobian associated with the generalized-coordinate formulation. Consequently, the arithmetic is comparatively reduced.

Three additional coordinate systems are used to complement the physical spherical system for the purpose of interrelating the velocity vector components. They are referred to as wind, body, and intrinsic frames and shown in Fig. 2. The unit vectors are defined in Table 1.

Let curvilinear coordinates (ξ,η,ζ) be $\xi = \pi - \theta$, $\eta = r$, and $\zeta = \phi$. Then, the unit vectors (i,j,k) and (I,J,K) shown in Fig. 2 are related by

$$d\vec{r} = I\,dX + J\,dY + K\,dZ = i\,d\xi + j\,d\eta + k\,d\zeta$$

and

$$X = \eta \sin \xi \cos \zeta,\quad Y = \eta \sin \xi \sin \zeta,\quad Z = -\eta \cos \xi$$

The relationships are given in Table 1. If the body surface is represented by $f = \eta - B(\xi,\zeta) = 0$, then its outward normal gradient is $\nabla f = j - iB_\xi/B - kB_\zeta/(B \sin \xi)$. After normalization of ∇f, $n = \nabla f/|\nabla f|$, the tangent and binomial vectors, also shown in Fig. 1, are obtained from $t = n \times k$ and $b = t \times n$. The intrinsic frame on the shock $g = \eta - S(\xi,\zeta) = 0$ is defined likewise, except that n is inward. Note that all unit vectors follow the right-hand rule.

The body configuration is prescribed analytically in terms of a series of conics or their degenerated form assuming symmetry with respect to the Z-axis, or on a number of X-Y planes away from a spherical cap. The cylindrical (r,ϕ,Z) coordinates are used to define the body, then the independent variables are changed to (ξ,η,ζ).

2.2 Equations in Computation Space

The conservative laws of a single-component, compressible, viscous flow are given in vector notation as follows.

$$u_t + f_x + g_y + h_z + r = 0 \qquad (1)$$

where $x = \xi$, $y = \eta(S,B)$, $z = \zeta$, $u = h_1h_3\bar{u}$, $f = h_3\bar{f}$, $g = y_\xi h_3\bar{f} + y_\eta h_1h_3\bar{g} + y_\zeta h_1\bar{h}$, $h = h_1\bar{h}$, $r = \bar{r}$, $h_1 = \eta$, $h_3 = \eta \sin \xi$, and metrics y_ξ, y_η, and y_ζ are held nondifferentiable with respect to y. Note that y_t is absent, even though $S = S(\xi,\zeta,t)$. The convective and diffusive fluxes are of the following expression.

$$\bar{u} = \begin{bmatrix} \rho \\ \rho u \\ \rho v \\ \rho w \\ \rho\varepsilon \end{bmatrix}, \quad \bar{f} = \begin{bmatrix} \rho u \\ \rho u^2 + \pi_{\xi\xi} \\ \rho uv + \pi_{\xi\eta} \\ \rho uw + \pi_{\xi\zeta} \\ \rho u\varepsilon + \Phi_\xi \end{bmatrix}, \quad \bar{g} = \begin{bmatrix} \rho v \\ \rho vu + \pi_{\eta\xi} \\ \rho v^2 + \pi_{\eta\eta} \\ \rho vw + \pi_{\eta\zeta} \\ \rho v\varepsilon + \Phi_\eta \end{bmatrix},$$

$$\bar{h} = \begin{bmatrix} \rho w \\ \rho wu + \pi_{\zeta\xi} \\ \rho wv + \pi_{\zeta\eta} \\ \rho w^2 + \pi_{\zeta\zeta} \\ \rho w\varepsilon + \Phi_\zeta \end{bmatrix}, \quad \bar{r} = \begin{bmatrix} 0 \\ h_3(h_1)_\eta(\rho uv + \pi_{\xi\eta}) - (h_3)_\xi(\rho w^2 + \pi_{\zeta\zeta}) \\ -h_1(h_3)_\eta(\rho w^2 + \pi_{\zeta\zeta}) - h_3(h_1)_\eta(\rho u^2 + \pi_{\xi\xi}) \\ (h_3)_\xi(\rho wu + \pi_{\zeta\xi}) + h_1(h_3)_\eta(\rho wv + \pi_{\zeta\eta}) \\ 0 \end{bmatrix}$$

Equation (1) is used everywhere except on the Z-axis (Fig. 1), wherein $w = 0$ and $\xi = 0$ by definition. The exact form of the governing equation is

$$u_t + f_x + g_y + r = 0 \qquad (2)$$

where

$$u = \bar{u}, \; f = (2 - u^*/u)\,\bar{f} + \bar{h}_Z - u\,\bar{u}^*, \; g = y_\xi f + y_\eta h_1 \bar{g}$$

$$\bar{f} = \begin{bmatrix} \rho u \\ \rho u^2 - p + \pi_{\xi\xi} \\ \rho uv + \pi_{\xi\eta} \\ 0 \\ \rho u\varepsilon + \Phi_\xi \end{bmatrix}, \quad \bar{u}^* = \begin{bmatrix} \rho^* \\ \rho^* u^* \\ \rho^* v^* \\ 0 \\ \rho^*\varepsilon^* - p^* \end{bmatrix},$$

$$r = \begin{bmatrix} \rho v \\ 2(\rho uv + \pi_{\eta\xi}) \\ \rho(-u^2 + v^2) + \pi_{\eta\eta} - \pi_{\xi\xi} - \pi_{\eta\zeta} \\ 0 \\ \rho v\varepsilon + \Phi_\eta \end{bmatrix}$$

$$u^* = u(0,\eta,0), \; w = 0$$

The derivation of Eq. (2) is given in Appendix A.

In Eqs. (1) and (2), complete stress tensor and heat-flux components are shown, but the order-of-magnitude analysis applied to the same equations on body intrinsic coordinates indicates that $\pi_{\eta\xi}$ and $\pi_{\eta\zeta}$ are the only important ones in f, g, h, and r. It should be pointed out that $\pi_{\eta\xi}$ in r cannot be eliminated at all.

In the preceding expressions, ρ, u,v,w, and ε are density, velocity components in (ξ,η,ζ), and total energy, respectively. Variables of Eqs. (1) and (2) are made dimensionless from

$$\rho = \rho'/\rho'_\infty, u = u'/\sqrt{p'_\infty/\rho'_\infty}, \varepsilon = \varepsilon'/p'_\infty/\rho'_\infty, p = p'/p'_\infty,$$

$$T = T'/T'_\infty, \xi = \xi'/R_N, t = t'\sqrt{p'_\infty/\rho'_\infty}/R_N$$

The primed variables indicate dimensional quantities, whereas the subscript ∞ refers to free-stream condition; R_N is the nose radius, and p,T are, respectively, pressure and temperature.

Two components of the stress tensor, π_{ij} and q_i, are defined in orthogonal coordinates as follows:

$$\left.\begin{aligned} \pi_{\xi\xi} &= p - \frac{\sqrt{\gamma_\infty}M_\infty}{Re}\left(e_{\xi\xi} - \frac{1}{3}(e_{\xi\xi} + e_{\eta\eta} + e_{\zeta\zeta})\right) \\ e_{\xi\xi} &= 2\left(\frac{1}{h_1}\frac{\partial u}{\partial \xi} + \frac{v}{h_1 h_2}\frac{\partial h_1}{\partial \eta}\right) \\ q_\xi &= -\frac{\sqrt{\gamma_\infty}M_\infty\gamma}{(\gamma - 1)P_R Re}\frac{1}{h_1}\frac{\partial T}{\partial \xi} \end{aligned}\right\} \qquad (3)$$

The Stokes assumption has been used to derive formulas for the stress tensor. Parameters in Eq. (3) are the ratio of specific heats γ, Mach number M, Reynolds number Re, and Prandtl number P_R. Definitions of Re and P_R are given by $Re = \rho_\infty V_\infty R_N/\mu$ and $P_R = C_p\mu/K$; V_∞ denotes free-stream speed, μ and K the coefficients of viscosity and thermal conductivity, and C_p the specific heat at constant pressure. These are dimensional quantities. Finally, the thermal equation of state

$$p = \rho RT \tag{4}$$

is required to complete the system of governing equations. In this equation, R refers to the gas constant. The number of dependent variables is limited to six since $\varepsilon = e + 0.5(u^2 + v^2 + w^2)$ and the specific internal energy e can be related to T by the caloric equation of state $e = C_vT$, where C_v is the specific heat at constant volume, or by $e = e(p,\rho)$ for equilibrium air.

2.3 Mapping Functions

Equations (1) and (2) are dedicated to the flowfield calculation between the shock and the body. This calculation is accomplished by selecting a coordinate transformation equation such as $y = \bar{\eta} = (\eta - B)/(S - B)$, which implies that for a given ξ and ζ, η corresponds to equally spaced $\bar{\eta}$ varying from 0 to 1. The convenience of addressing a radial location within the shock layer can be extended to clustered locations of η by using any one of the three exponential functions

$$y = (\exp(\beta\bar{\eta}) - 1)/(\exp(\beta) - 1) \tag{5a}$$

$$y = \sinh(\beta\bar{\eta})/\sinh\beta \tag{5b}$$

$$y = \frac{\ln[(\beta + \bar{\eta})/(\beta - \bar{\eta})]}{\ln[(\beta + 1)/(\beta - 1)]} \tag{5c}$$

Hence, for a given set of y points, uneven distributions of η points can be defined. However, more cluster points toward the body often results in fewer points away from the shock. By comparing the characteristics due to different exponential functions, it is found that the last function from Tannehill(14) offers the most desirable clustering near $y = 1$ while maintaining an approximately linear relation $y \propto \bar{\eta}$ for $y < 0.8$.

As shown in Fig. 3, the degree of clustering is determined by the slope of $y_{\bar{\eta}}$ at $\bar{\eta} = 1$, which, in turn, is controlled by the parameter β. To find β for specified values of y' and $\bar{\eta}'$, a nonlinear equation

$$f(\beta) = y' \ln\frac{\beta + 1}{\beta - 1} + \ln\frac{\beta + \bar{\eta}'}{\beta - \bar{\eta}'} = 0$$

may be solved by means of Newton's technique.

$$\beta^{n+1} = \beta^n + (\beta_y)^n(y' - y'^n)$$

where

$$y_\beta = +2\left[\frac{1}{\beta^2 - 1} + \frac{\bar{\eta}'}{\beta^2 - \bar{\eta}'^2}\right]\Big/\ln\left(\frac{\beta + 1}{\beta - 1}\right)$$

2.4 Boundary Conditions

Flow variables along $\eta = S(\xi,\zeta)$ as given by Eqs. (1) and (2) are made to satisfy the Rankine-Hugoniot (RH) relations by introducing a local shock speed jS_t at (ξ,ζ). Thus, the incoming free-stream velocity $\vec{V}_\infty$ and the flow vector immediately downstream of the shock $\vec{V}$ are modified by the shock speed in the stationary intrinsic frame. Let prime refer to the intrinsic frame. Then

$$\vec{V}'_\infty = \vec{V}_\infty - jS_t, \vec{V}' = \vec{V} + jS_t$$

where
$$\vec{V}_\infty = IV_\infty \sin(\alpha - \alpha_T) + KV_\infty \cos(\alpha - \alpha_T)$$
$$\vec{V} = IU_\infty + KW_\infty = iu_\infty + jv_\infty + kw_\infty$$

Table 1 can be used to relate u_∞, v_∞, and w_∞ to U_∞ and W_∞.

An iteration procedure (secant formula) is used to find S_t by matching $\vec{V}'$ with $n_1u + n_2v + n_3w$, whereas $\vec{V}'$ is governed by the RH equations shown in the following:

$$\left.\begin{aligned}
&n\cdot(\vec{V}'_\infty - \rho\vec{V}') = 0\\
&(n\cdot\vec{V}'_\infty)^2 + 1 = \rho(n\cdot\vec{V}')^2 + p\\
&b\cdot(\vec{V}'_\infty - \vec{V}') = 0\\
&t\cdot(\vec{V}'_\infty - \vec{V}') = 0\\
&h_\infty + 0.5V'^2_\infty = h + 0.5V'^2
\end{aligned}\right\} \tag{6}$$

For a given S_t, another round of iterations is needed to solve Eq. (6). The iterated variable is the density ratio across the shock for an ideal-gas model; the process converges within three to four iterations. For an equilibrium-air model, the iterated variable is the enthalpy, which is available as a function of $h = h(p,\rho)$ in a curve-fit subroutine in Ref. 12.

The wall boundary $\eta = B(\xi,\zeta)$ imposes different types of conditions depending on whether the flow is inviscid or viscous. In accordance with the mathematical characteristics of a parabolic equation, either pressure or density needs to be calculated, whereas other variables may be specified. Thus, in the viscous calculation, no-slip velocity and isothermal or adiabatic temperature are specified on the wall. These conditions are simply $\vec{V} = 0$, $e = e_w$ or $n \cdot \nabla e = 0$. For the hyperbolic equation, only one condition is allowed; therefore, $n \cdot \vec{V} = 0$ is generally required. In an attempt to ensure that the flow variables still satisfy conservative laws, the velocity components parallel to the wall, $V'_b = b \cdot \vec{V}$ and $V'_t = t \cdot \vec{V}$, are multiplied by a factor $\vec{V} \cdot \vec{V} / (V'^2_b + V'^2_t)$, then converted back to the (ξ,η,ζ) frame by

$$u = b_1 V_b + t_1 V_t,\ v = b_2 V_b + t_2 V_t,\ w = b_3 V_b \qquad (7)$$

The pressure and density as computed from Eqs. (1) and (2) remain unchanged.

The outflow boundary, specified as a cone generator with $\xi = \xi_{max}$, is to be located well within the supersonic flow and on the portion of the body where a rapid change of flow direction is not expected. Inside the viscous layer, when the outflow is subsonic, one-point extrapolation is used. Otherwise, the flow variables are obtained by a linear two-point extrapolation of interior results. On the pitch plane $Y = 0$, the flow variables are to satisfy $k \cdot \nabla u = 0$, where $u = p$, ρ, e, u, and v, and to satisfy $k \cdot \nabla (k \cdot \nabla w) = 0$.

The remaining boundary $\xi = 0$, a singular line in physical space, necessitates rigorous analysis. The best approach to handling this boundary is to solve the governing equations in special form (Eq. (2)) on the same basis as for the interior region. But Eq. (2) is only to be used once in conjunction with flow variables on the pitch plane. Then, flow variables on other meridional planes are obtained from

$$\rho(0,\eta,\zeta) = \rho(0,\eta,0)$$

$$u(0,\eta,\zeta) = u(0,\eta,0)\cos\zeta$$

$$v(0,\eta,\zeta) = v(0,\eta,0)$$

$$w(0,\eta,\zeta) = -u(0,\eta,0)\sin\zeta$$

$$e(0,\eta,\zeta) = e(0,\eta,0)$$

2.5 Initial Flow Approximation

The present approach to solving blunt-body problems is a special class of time-dependent method that retains the unsteady derivative of the governing equations but merely simulates pseudo-physical phenomena. In a truly numerical simulation of flow over the body, it is often necessary to start the time-dependent calculation at the instant the body is immersed into the free stream, and the calculation continues until the steady state is reached. At best, this simple procedure is physically sound; however, it is not computationally robust if the body imparts a great amount of disturbance to the free stream, such as in a hypersonic stream. Hence, the code uses an alternate procedure that prescribes the essential features of the inviscid flowfield and starts the calculation with a rather crude initial approximation.

To accommodate the various shock shapes and body configurations displayed in Fig. 1, a reasonably accurate procedure for inviscid flow calculations has been implemented into the code. The stagnation properties and location are determined on the pitch plane from $n \cdot \vec{V} = 0$, then, taking into account the angle of attack, a body angle is found to be equal to

$$\theta = \cos^{-1}\Big(n \cdot t \cos(\alpha - \alpha_T) + n \cdot k \sin(\alpha - \alpha_T)\Big)$$

With θ, a distribution of Mach number is estimated to be $M = |2 \sin\theta|$ or $M = 1 + |\sin\theta|$ for $\theta \geq \pi/4$. Using the Mach distribution and the stagnation properties, isentropic expansion formulas can be applied to calculate the remaining flow variable on the body. This procedure is found to be more versatile than the one based on the Newtonian pressure and the conservation law of total enthalpy on the wall, e.g.

$$p_w = 1 + (n \cdot \vec{V}_\infty)^2$$

$$H_w = h_\infty + 0.5V_\infty^2 = h_w + 0.5\Big(\vec{V}_\infty - n(n \cdot \vec{V}_\infty)\Big)^2$$

$$\rho_w = \gamma p_w / (\gamma - 1) h_w$$

The flow vector tangent to the wall is readjusted in accordance with Eq. (6) discussed in sec. 2.4. The shock standoff distance at the stagnation point is obtained simply from $\delta_o = 0.15 M_\infty / (M_\infty - 1)^{1.1}$; δ_o is multiplied by 0.5 if an equilibrium-air model is used.

The complete shape is estimated from $S = B + \delta_o \exp(a|\xi + \alpha \cos \zeta|)$ for Fig. 1a, $S = B + \delta_o(1 + a(2/\pi(\xi - \alpha_T \cos \zeta))^2)$ for Fig 1c, and $S = B + \delta_o(1 + a \cos \xi)$ for Fig. 1b, where a is an input parameter. The shock location takes the following form for $M \gtrsim 1$, $S = d/(\cos \xi + 1/c)$, a quadratic curve intersecting $\xi = 0$ and $\pi/2$ lines; d and c are parameters to be determined for each case considered. Once the shock is known, the stationary RH equations are used to calculate shock variables which are used with the wall variables to determine the variables inside the shock layer by linear interpolations.

For viscous flow calculations, it is recommended to start from a nearly converged inviscid calculation for which the major portion of the shock layer is well established. In this way, a substantial reduction of computation time can be accomplished.

2.6 Wall Shear, Heat Flux, and *L/D* Calculations

Vector components of velocity, stress, and heat flux can be easily obtained in the wall intrinsic frame from those in the spherical frame. With reference to Table 1, a transformation matrix *T* may be defined to relate the components in both frames by

$$T = \begin{bmatrix} n_1 & n_2 & n_3 \\ t_1 & t_2 & 0 \\ b_1 & b_2 & b_3 \end{bmatrix}$$

such that

$$\begin{pmatrix} u_n \\ u_t \\ u_b \end{pmatrix} = T \begin{pmatrix} u \\ v \\ w \end{pmatrix} \text{and} \begin{pmatrix} q_n \\ q_t \\ q_b \end{pmatrix} = T \begin{pmatrix} q_\xi \\ q_\eta \\ q_\zeta \end{pmatrix}$$

Likewise, a tensor can be transformed accordingly by

$$\pi' = T \pi T^T \tag{8}$$

where the prime denotes the intrinsic frame and superscript *T* denotes transpose of the transformation matrix. The expanded expression of streamwise and crossflowwise shear stress components and of the body-normal heat-flux component are as follows:

$$\pi_{nt} = n_1(t_1\pi_{\xi\xi} + t_2\pi_{\xi\eta}) + n_2(t_1\pi_{\eta\xi} + t_2\pi_{\eta\eta}) + n_3(t_1\pi_{\zeta\xi} + t_2\pi_{\zeta\eta})$$

$$\pi_{nb} = n_1(b_1\pi_{\xi\xi} + b_2\pi_{\xi\eta} + b_3\pi_{\xi\zeta}) + n_2(b_1\pi_{\eta\xi} + b_2\pi_{\eta\eta} + b_3\pi_{\eta\zeta})$$

$$+ n_3(b_1\pi_{\zeta\xi} + b_2\pi_{\zeta\eta} + b_3\pi_{\zeta\zeta})$$

$$q_n = n_1 q_\xi + n_2 q_\eta + n_3 q_\zeta$$

The drag and lift are obtained by integrating the pressure and shear stress on the body surface from

$$\left.\begin{aligned} D &= \int_0^\pi \int_0^{\xi_{max}} \left(n\cdot K\pi_{nn} + t\cdot K\pi_{nt} + b\cdot K\pi_{nb} \right) d\sigma \\ L &= \int\int \left(n\cdot I\pi_{nn} + t\cdot I\pi_{nt} + b\cdot I\pi_{nb} \right) d\sigma \end{aligned}\right\} \tag{9}$$

where $d\sigma = B^2 \sin\xi\, d\xi\, d\zeta$ and the scalar products are, for example,

$$n\cdot K = n_1 \sin\xi - n_2 \cos\xi$$

$$n\cdot I = n_1 \cos\xi \cos\zeta + n_2 \sin\xi \cos\zeta - n_3 \sin\zeta$$

If α and α_T are nonzero, the drag and lift forces can be obtained in the wind frame from

$$\overline{L} = L \cos(\alpha - \alpha_T) - D \sin(\alpha - \alpha_T)$$

$$\overline{D} = L \sin(\alpha - \alpha_T) + D \cos(\alpha - \alpha_T)$$

3. Implicit Difference Method

3.1 Difference Approximations

The computation space (x,y,z) is discretized into a three-dimensional network of grid points, which are defined by

$$x_m = (m-2)\Delta x,\ y_n = (n-2)\Delta y,\ z_\ell = (\ell - 2)\Delta z \tag{10}$$

with $\Delta x = x_{max}/(mc - 2)$, $\Delta y = 1/(nc - 2)$, $\Delta z = \pi/(lc - 2)$, and $m = 1, 2, \ldots mc$, $n = 2, 3, \ldots nc$, and $\ell = 1, \ldots lcp$, where $lcp = lc + 1$. The subscripts m and ℓ cover a range of grid points beyond the computation domain (Fig. 2) in order to incorporate the boundary conditions. Equation (10) indicates that any point in the computation space can be addressed by the intersection of three independent families of coordinate lines, but the metrics and the dependent variables still require three-dimensional arrays such as $\rho_{n,m,\ell} = \rho(x_m, y_n, z_\ell)$ and $h_{n,m,\ell} = h(x_m, y_n, z_\ell)$.

The partial derivatives are approximated by central- and one-sided-difference formulas

$$\delta_x \rho = (\rho_{m+1} - \rho_{m-1})/2\,\Delta x$$

$$\delta_x^{\,+}\rho = (\rho_{m+1} - \rho_m)/\Delta x,\ \delta_x^{\,-}\rho = (\rho_m - \rho_{m-1})/\Delta x$$

wherein subscripts n and ℓ are excluded for brevity. The one-sided quotients and subscripts $m \pm 1/2$ are used primarily for the diffusive flux terms in Eqs. (1) and (2). For example,

$$\delta_x(\mu u_x/h_1) = \left[(\mu/h_1)_{m+1/2}(\delta_x^{\,+}u)_m - (\mu/h_1)_{m-1/2}(\delta_x^{\,-}u)_m \right]/\Delta x$$

$$\delta_z(\mu h_1 y_\eta (u/h_1)_y) = \Big[(\mu h_1 y_\eta)_{\ell+1/2}\,\delta_y(u/h_1)_{\ell+1/2}$$

$$- (\mu h_1 y_\eta)_{\ell-1/2}\,\delta_y(u/h_1)_{\ell-1/2} \Big]/\Delta z$$

where

$$\delta_y(u/h_1)_{\ell\pm1/2} = \Big[(u/h_1)_{n+1,\ell\pm1} - (u/h_1)_{n-1,\ell} + (u/h_1)_{n+1,\ell}$$

$$- (u/h_1)_{n-1,\ell\pm1} \Big]/2\,\Delta y$$

Special expressions for diffusive terms are needed on $x = 0$ wherein $h_3 = 0$, but details will not be presented here.

3.2 ADI Factorization Technique

The resultant finite-difference counterpart of Eq. (1) is

$$\delta_t^+ u + \delta_x f + \delta_y g + \delta_z h + r_{n,m,\ell} = 0 \tag{11}$$

where

$$\delta_t^+ u = (u_{n,m,\ell}^{k+1} - u_{n,m,\ell}^{k})/\Delta t + 0(\Delta t^2)$$

$$\delta_x f = (f_{n,m+1,\ell}^{k+1} - f_{n,m-1,\ell}^{k+1})/2\,\Delta x, \text{ etc.}$$

The spatial approximations are solved simultaneously with the unknown vector $u_{n,m,\ell}^{k+1}$ to allow greater changes of $\delta_t u^+$ and, hence, to result in a faster rate of convergence from initial approximations to the final solution. A factorization technique due to Beam and Warming(8) which emphasizes the noniterative nature of the well-established ADI method and solves for the incremental vector of the conservative variable u has been adopted and modified. In this version, because the primitive variables $v = (\rho, u, v, w, e)^T$ are used, the Jacobian matrices have simpler expression and involve less arithmetic. The solution procedure comprises five steps.

$$\begin{gathered}
\tau \Delta u_{n,m,\ell}^{k} = -\delta_x f^k - \delta_y g^k - \delta_z h^k - r_{n,m,\ell}^{k} \\
\left(\tau I + \delta_x A - \delta_{xx}(D + \tau d_I I)\right)\Delta v_{n,m,\ell}^{*} = \tau P^{-1}(\Delta u_{n,m,\ell}^{k} - d_e\, \delta^4 u_{n,m,\ell}^{k}) \\
\left(\tau I + \delta_y B - \delta_{yy}(E + \tau d_I I)\right)\Delta v_{n,m,\ell}^{**} = \tau \Delta v_{n,m,\ell}^{*} \\
\left(\tau I + \delta_z C - \delta_{zz}(F + \tau d_I I)\right)\Delta v_{n,m,\ell}^{k+1} = \tau \Delta v_{n,m,\ell}^{**} \\
v_{n,m,\ell}^{k+1} = v_{n,m,\ell}^{k} + \Delta v_{n,m,\ell}^{k+1}
\end{gathered} \tag{12}$$

where τ is the inverse of the local Δt multiplied by a constant Courant number, and d_I and d_e are the implicit and explicit damping coefficients to be discussed later. Jacobian matrices P, A, B, C, D, E, and F have analytical expressions. Each of the three equations in the middle of Eq. (12) represents a tridiagonal system of linear equations with 5 by 5 matrix coefficients. A standard algorithm has been used earlier in Ref. 9.

It is seen in Eq. (12) that the first step is to find the residual explicitly, then to smooth or to filter out the localized errors in $\Delta u_{n,m,\ell}^{k}$ by subsequent implicit steps performed along each coordinate. Obviously, the implicit calculations are not needed for numerical stability consideration alone if $\Delta t_{n,m,\ell}$ meet the Courant-Friedrich-Lewy (CFL) criterion, or any step can be deleted if $(\Delta t_i)_{min} > CN(\Delta t_{n,m,\ell})_{min}$, where i = n, m, or ℓ and CN denotes the Courant number. Nevertheless, the primary function of implicit solutions seems to be more in the acceleration of the overall rate of convergence than in maintaining solution stability. Numerical experiments have suggested that implicit solution is even preferable (without concern in computation cost) to the explicit solution because the effect of boundaries can be transmitted across the entire line. To illustrate the manner in which boundary conditions are incorporated into the tridiagonal system of equations, the third equation of (12) is rewritten in algebraic form for index n.

$$\left.\begin{aligned}
b_2 \Delta v_2^{**} + c_2 \Delta v_3^{**} &= \Phi_2^{*} \\
a_n \Delta v_{n-1}^{**} + b_n \Delta v_n^{**} + c_n \Delta v_{n+1}^{**} &= \Phi_n^{*} \\
a_{ncm} \Delta v_{ncm-1}^{**} + \bar{b}_{ncm} \Delta v_{ncm}^{**} &= \Phi_{ncm}^{*}
\end{aligned}\right\} \tag{13}$$

where

$$a_n = \frac{-1}{2\Delta y}\left(B_{n-1} + \frac{2}{\Delta y}(E_{n-1} + \tau d_I)\right)$$

$$b_n = \tau_n + \frac{2}{(\Delta y)^2}(E_n + \tau d_I)$$

$$c_n = \frac{1}{2\Delta y}\left(B_{n+1} - \frac{2}{\Delta y}(E_{n+1} + \tau d_I)\right)$$

$$\begin{aligned}
\bar{b}_{ncm} &= b_{ncm} \quad \text{for } u, v, w \\
&= b_{ncm} + c_{ncm} T_{ncm} / T_{nc} \quad \text{for } \rho
\end{aligned}$$

Equation (13) solves for Δv_n^{**} from n = 2 through $ncm = nc - 1$; on the wall, Δu_{nc} = Δv_{nc} = Δw_{nc} = Δe_{ncm} = 0 for no-slip and isothermal conditions and p_{nc} = p_{ncm} implies $\Delta \rho_{nc}$. It is noteworthy to point out that implementation of boundary conditions is relatively inconvenient for conservative variables.

3.3 Jacobian Matrices

The nonlinear difference equation (11) is linearized according to Newton's method prior to the factoring of spatial operators into Eq. (12). The iteration steps of solving a set of nonlinear equations can be minimized if the Jacobian matrices are exact and updated at each step. By definition, $\Delta\bar{u} = P\,\Delta v$, $\Delta f = PA\,\Delta v$, $\Delta g = PB\,\Delta v$, $\Delta h = PC\,\Delta v$, $\Delta f_v = PD\,\Delta(\delta v_x)$, $\Delta g_v = PE\,\Delta(\delta v_y)$, $\Delta h_v = PF\,\Delta(\delta v_z)$, where subscript v refers to the diffusive fluxes, and x, y, and z denote the respective derivatives. Note that the linearized difference equation contains no Jacobian matrices due to mixed derivatives, because of the nature of the ADI factorization technique.

$$P^{-1} = \frac{1}{\rho}\begin{bmatrix} \rho & 0 & 0 & 0 & 0 \\ -u & 1 & 0 & 0 & 0 \\ -v & 0 & 1 & 0 & 0 \\ -w & 0 & 0 & 1 & 0 \\ \varepsilon - 2e & -u & -v & -w & 1 \end{bmatrix}$$

$$A = h_3\begin{bmatrix} u & \rho & 0 & 0 & 0 \\ ge/\rho & u & 0 & 0 & g \\ 0 & 0 & u & 0 & 0 \\ 0 & 0 & 0 & u & 0 \\ 0 & p/\rho & 0 & 0 & u \end{bmatrix}, C = h_1\begin{bmatrix} w & 0 & 0 & \rho & 0 \\ 0 & w & 0 & 0 & 0 \\ 0 & 0 & w & 0 & 0 \\ ge/\rho & 0 & 0 & w & g \\ 0 & 0 & 0 & p/\rho & w \end{bmatrix}$$

$$B = h_3\begin{bmatrix} y_\xi u + h_1 y_\eta v + h_1 y_\zeta u/h_3 & y_\xi \rho & h_1 y_\eta \rho & h_1 y_\zeta \rho/h_3 & 0 \\ y_\xi ge/\rho & y_\xi u + h_1 y_\eta v + h_1 y_\zeta w/h_3 & 0 & 0 & y_\xi g \\ h_1 y_\eta ge/\rho & 0 & y_\xi u + h_1 y_\eta v + h_1 y_\zeta w/h_3 & 0 & h_1 y_\eta g \\ h_1 y_\zeta ge/\rho h_3 & 0 & 0 & y_\xi u + h_1 y_\eta v + h_1 y_\zeta w/h_3 & h_1 y_\zeta g/h_3 \\ 0 & y_\xi p/\rho & h_1 y_\eta p/\rho & h_1 y_\zeta p/\rho h_3 & y_\xi u + h_1 y_\eta v + h_1 y_\zeta w/h_3 \end{bmatrix}$$

$$D = \frac{h_3}{\rho h_1}\begin{bmatrix} 0 & 0 & 0 & 0 & 0 \\ 0 & \lambda + 2\mu & 0 & 0 & 0 \\ 0 & 0 & \mu & 0 & 0 \\ 0 & 0 & 0 & \mu & 0 \\ 0 & 0 & 0 & 0 & g\kappa \end{bmatrix}, F = \frac{h_1}{\rho h_3}\begin{bmatrix} 0 & 0 & 0 & 0 & 0 \\ 0 & \mu & 0 & 0 & 0 \\ 0 & 0 & \mu & 0 & 0 \\ 0 & 0 & 0 & \lambda + 2\mu & 0 \\ 0 & 0 & 0 & 0 & g\kappa \end{bmatrix}$$

$$E = \frac{h_3}{\rho}\begin{bmatrix} 0 & 0 & 0 & 0 & 0 \\ 0 & y_\xi^2(\lambda + 2\mu)/h_1 + y_\eta^2 \mu h_1 + h_1 y_\zeta^2 \mu/h_3^2 & h_1 y_\xi y_\eta(\lambda + \mu) & h_1 y_\xi y_\zeta(\lambda + \mu)/h_3 & 0 \\ 0 & h_1 y_\eta y_\xi(\lambda + \mu) & y_\xi^2/h_1 + h_1 y_\eta^2(\lambda + 2\mu) + h_1 y_\zeta^2 \mu/h_3^2 & h_1^2 y_\eta y_\zeta(\lambda + \mu)/h_3 & 0 \\ 0 & h_1 y_\zeta y_\xi(\lambda + \mu)/h_3 & h_1^2 y_\zeta y_\eta(\lambda + \mu)/h_3 & y_\xi^2 \mu/h_1 + h_1 y_\eta^2 \mu + h_1 y_\zeta^2(\lambda + 2\mu)/h_3^2 & 0 \\ 0 & 0 & 0 & 0 & \begin{matrix} g(y_\xi^2/h_1 + h_1 y_\eta^2 \\ + h_1 y_\zeta^2/h_3^2)\kappa \end{matrix} \end{bmatrix}$$

where $g = \gamma - 1$ and $\gamma = 1 + p/(\rho e)$ for both ideal-gas and equilibrium-air models.

3.4 Numerical Damping and Time Increment

Two types of damping terms are included in Eq. (12); a second-order term with constant value is used in the implicit operators, whereas a mixture of both second- and fourth-order terms is used in the explicit operators. The implicit damping terms are of the following form.

$$-d_I(\delta_{xx} + \delta_{yy} + \delta_{zz})\Delta v^{k+1}$$

Thus, this value enhances the diagonal dominance of the matrix and effectively extends the range of CN numbers. Although there is discernible lag of convergence history initially when the implicit damping is used, the convergence rate is faster as the solution reaches the asymptotic state. The best aspect of all is that the final results are nearly independent of d_I.

The use of explicit damping terms, however, exerts a profound effect on the solution stability and accuracy, because the added numerical dissipations become a permanent part of Eq. (12). The positive aspect is to smooth out spurious oscillation of results caused by the indiscriminating difference across flow gradients; the negative shortcomings are that they tend to mingle with the physical dissipation and markedly change the natural phenomena. For the blunt-body flowfield computation, the explicit damping terms can be selectively used and are beneficial rather than pernicious to the final solution. The second-order terms are only used for the inviscid portion of the shock layer. They consist of an expression giving a blanket smoothing and another expression depending on the pressure gradient, such as

$$+d_e(\delta_{xx} + \delta_{yy} + \delta_{zz})u^k + d_p(\delta_{xx} + \delta_{yy} + \delta_{zz})u^k$$

where, for $y < c_3$, $d_{e,2} = 0.02$ to 0.2, $d_p = |\delta_x{}^2 p/(4p)|$, and c_3 is a parameter delineating the boundary layer from the inviscid shock-layer flow. The fourth-order damping terms are used for the entire domain excluding the points on and adjacent to the boundaries. They are of the following form.

$$-d_e(\delta_x^4 + \delta_y^4 + \delta_z^4)u^k$$

where $d_{e,4} = \min\,(\Delta t, d_{e,2})$.

The time increment $\Delta t = 1/\tau$ in Eqs. (11) and (12) is a multiple of $(\Delta t)_{min}$ given by the CFL conditions for stability.

$$\Delta t = CN(\Delta t_{min}) = \frac{CN \min\,(\Delta\eta, \eta\,\Delta\xi, \eta \sin\xi\,\Delta\zeta)}{\min 1.5\left(a + (u^2 + v^2 + w^2)^{1/2}\right)_{n,m,\ell}} \qquad (14)$$

where a is the speed of sound. The Courant number CN is greater than unity but its magnitude depends partly on the values of d_I and d_e. It is seen that the fourth- and second-order damping on the right-hand side are independent of t, but the damping on the left-hand side as well as τ affects the diagonal dominance of the matrix. The allowable CN is also determined in part by the closeness of initial approximations to the solution; a smaller value is often needed at the beginning of the iterations, then a larger value is used later to optimize the convergence rate. If the maximum incremental variable of $\Delta\rho/\rho$ is used to gauge CN for the next iteration, then Δt is heuristically controlled by the outcome of each iteration. Therefore

$$\Delta t = CN(\Delta t)_{min}/(1 + \varepsilon)$$

where $\varepsilon = \max\,(\Delta\rho/\rho)_{n,m,\ell}$. The local-time increment for a constant CN

$$\Delta t_{n,m,\ell} = \frac{CN(\Delta\eta, \eta\,\Delta\xi, \eta \sin\xi\,\Delta\zeta)_{min}}{1.5\left[a_{n,m,\ell} + (u^2_{n,m,\ell} + v^2_{n,m,\ell} + w^2_{n,m,\ell})^{1/2}\right]} \qquad (15)$$

is to be used for all grid points in Eq. (12). However, the shock position is still updated by

$$S^{k+1}_{m,\ell} = S^k_{m,\ell} + (S_t)_{m,\ell}\,\Delta t \qquad (16)$$

The shock speed is smoothed before entering in Eq. (16) by

$$(S_t)_{m,\ell} = 0.5\left((S_t)_{m-1,\ell} + (S_t)_{m,\ell}\right)$$

if $\xi + \alpha \cos\zeta > c_1$, where c_1 ranges from 0.5 to 0.9.

4. Code Capabilities and Limitations

As indicated in sec. 1, the code is developed to provide flowfield data for the body configurations shown in Fig. 1. The body contour may be given either analytically or by a lofting procedure. The contour is allowed to be indented, if a uniform x_m is considered adequate to resolve the mild changes of body curvature. A choice can be made between a perfect gas and equilibrium air, but the turbulent eddy viscosity has not been incorporated. The computation domain is preferably no greater than 45° in the angular span of the cone generator since the shock fitting becomes less accurate as the angle $\cos^{-1}(i \cdot V_\infty / |V_\infty|)$ decreases. The speed of the incoming flow is unrestricted for the perfect-gas solution; however, it may impede the accuracy of shock fitting because, with an additional shock speed introduced, the resultant temperature behind the shock could be higher than the range of the curve fit for equilibrium-air properties. The location of the coordinate origin also controls the size of domain which is required to cover the entire subsonic region inside the shock layer. For instance, with an angle of attack of 40°, the sonic line is found to extend as far as $3R_N$ from the nosetip. Higher flow incidence angle may cause the grid lines to intersect the shock and the body at excessively skewed angles and to give rise to computational errors. The configuration of Fig. 1a represents the nose of a high lift-to-drag (*L/D*) vehicle; hence, both nose and axial-plane data are needed as shown in Ref. 9. The configuration of Fig. 1b, suitable to start a method-of-characteristics solution, was considered in Ref. 2. The configuration illustrated by Fig. 1c has sonic shoulder of varying degrees of curvature and a wide-angle conic frontal surface. This type of body is being investigated for aerobraking near the upper Earth atmosphere. The following discussion will highlight the parameters used to set up the computation.

The Euler code is robust and accurate while forgiving to the spatial resolution, CN number, and damping coefficients. As long as the outflow boundary is well outside the subsonic zone, coarse grids of 5 by 12 by 0 and 10 by 12 by 7 for 2D and 3D cases, respectively, are sufficient to yield results accurate to the third digit. The calculation is stable with $CN = 3$ to 15 for global-time increment and $CN = 3$ to 6 for local-time increment. The time steps are between $k = 100$ to 300 to achieve convergence. The criteria of solution convergences are based on the maximum incremental variable $\varepsilon = \max |\Delta\rho/\rho|$, the maximum range of shock speed $\bar{S}_t = |\max S_t - \min S_t|$, and the maximum deviation of total enthalpy ΔH. For coarse grid solution, $0.001 \le \varepsilon \le 0.01$, $0.01 \le \bar{S}_t \le 0.1$, and $\Delta H \le 0.005$ are considered sufficient. The criteria can be lowered according to the reduced grid spacing. The seemingly high threshold for $\bar{S}_t$ is due to the inaccuracy of shock fitting near the upper end of the shock. It should be noted that the corresponding root-mean-square (rms) value of S_t is generally one order of magnitude less than $\bar{S}_t$.(15) For most calculations, the time increment and damping coefficients are observed to exert noticeable effect on the converged results; it is a recognized characteristic associated with the ADI technique. The explicit damping terms enhance the computational stability as well as the code robustness. Both second- and fourth-order damping are used and an additional shock-speed-smoothing scheme is introduced to ensure that the shock and flow variables have no anomalous oscillation. The damping coefficient $d_e \le 0.1$ is recommended for inviscid calculations. The effect of damping helps to expel the errors outside the domain, as ΔH may vary from 0.2 to 0.005 during the time integration. If ΔH has a constant level of error, a slightly greater d_e may be needed.

The viscous calculations can be performed from the results of their inviscid counterparts or, alternatively, by going through a straightforward coarse-to-fine grid sequence. Both have been used and found to be cost-effective. After interpolating the coarse inviscid grid to grids of 28 by 10 by 0 or 28 by 12 by 7 on a nonuniform grid exponentially stretched toward the shock, the grid spacing adjacent to the wall is estimated by $\Delta y = 0.2R_N/(\beta Re)^{1/2}$, where β is a parameter equal to $(T_{st}/T_w)^{1/2}$; the subscripts *st* and *w* refer to the stagnation and the wall, respectively. As more grid points are packed toward the wall, sparse grid points are seen near the shock. To prevent shock-fitting errors caused by the stretched grid from accumulating, more than 28 points may be occasionally needed to maintain S_t to a negligible level. The grid spacing Δx and Δz is not as important to the accuracy unless around a sonic shoulder as in Fig. 1c or for the indented nose investigated in Ref. 10. One should be cautioned that the placement of the outflow line is more critical than for the inviscid calculation; placement is preferably on the axial plane, where flow is less accelerating than on other parts of the body. The local-time increment is advantageous to use since S_t is smaller while the rate of convergence for the heat-transfer and friction coefficients, C_H and C_F, respectively, is faster. The Courant number is in the range of $CN = 20$ to 35, a factor of 2 lower than that used for global-time increment. The criterion for convergence is the same as that for inviscid computations plus the check made to the values of C_H and C_F.

Although the 3D NS code has performed exceptionally well in terms of the grid points and integration steps used for the strongly asymmetric flowfield considered, surprises do occur in lack of convergence, solution smoothness, and accuracy of results. The remedies to overcome these difficulties are 1) reducing grid spacing and CN, 2) increasing d_e, and 3) selecting a different Z_o. The following section will demonstrate much of the usefulness and the versatility of the code for a wide range of practical problems.

5. Discussion of Sample Cases

Five problems have been selected to represent a partial spectrum of current interests; their free-stream conditions, computation domain, grid, and body shape are given in Table 2 in accordance with the required computational effort. All are laminar flow and isothermal wall, and the computation domain contains an axial plane at Z_o. Coarse grids were used so that a scalar computer such as Univac 1182 will have sufficient size and speed to execute simple 2D cases in time-sharing mode and 3D cases overnight. Before addressing each individual case, we will explore some basic issues that have revealed interesting and noteworthy observations, which are shared by the shock-fitting implicit numerical procedure for both Euler and Navier-Stokes codes.

The convergence rate, as expected, varies with the time increment even though the shock position is decoupled from the implicit calculation. Shown in Fig. 4a is the convergence history of the time integration for an inviscid flow over a sphere at $\alpha = 0°$ and $M = 5.94$ obtained with $CN = 3$, 9, and 15. This Naval Surface Weapon Center (NSWC) case is designated NSWC-1. Using global-time increment, the higher value of CN leads to lower value of $\bar{S}_t$ and ε over nearly all time steps except near $k = 200$. At the end of computation, both $\bar{S}_t$ and ε are seen to level off where the errors due to truncation, linearization, factorization, and numerical damping have reached equilibrium. Further calculations did not alter the level appreciably. The convergence history obtained from the calculations using local-time increment is plotted in Fig. 4b. Despite the lower $CN = 6$ value permitted by local-time increment, the rate of convergence is seen as rapidly decreasing as that in Fig. 4a for $CN = 15$ using global time. As marked in Figs. 4a and 4b, the shock standoff distance and the pressure on the stagnation point only differ by 1% from each other. Both cases (8 by 12) are considered very accurate for ΔH of less than 0.1%. Discernible advantages of accelerating the convergence process are noted for viscous flow computations. Figure 4c shows the convergence rate for both local- and global-time integration. The value of $\bar{S}_t$ is also smaller in local-time calculation. The convergence rate for global-time integration does not speed up as much as expected for $CN = 50$. Hence, local-time integration has been used for all results discussed later. The converged C_H value of 0.0042 compared favorably with the value 0.0043 obtained by Hsieh.(15)

The significance of using local time as opposed to global time is further exemplified by Fig. 5, wherein the shock speeds are compared. The local-time solution gives a uniformly lower shock speed than those obtained with global-time calculation. The greatest S_t occurs at $\xi = \pi/2$ for both cases. The error in $\bar{S}_t$, estimated by $|\bar{S}_t|/(\sqrt{\gamma} M_\infty)$, imposes little upstream influence because of its proximity to the outflow line. It is inherently associated with the finite-difference shock-fitting scheme that is an approximation to the original method-of-characteristics shock fitting advocated by Moretti.(2) Regardless of the error magnitude, the shock locations are very close to those shown in Ref. 1 for $M = 3$: $\delta_o = 0.229$ vs. 0.23 and $\delta_{\pi/2} = 1.04$ vs. 0.9. Another important observation is that the converged results obtained using different damping coefficient or CN values may not be in perfect agreement.

A comparison of C_H and C_F distributions between the NS and the boundary-layer (BL) results is shown in Fig. 6 for the Arnold Engineering Development Center (AEDC) case at $\alpha = 0°$. The inviscid and viscous pressure distributions are almost identical for this Re range. The NS code has predicted higher C_F over the entire wall, but yielded a C_H distribution that coincided with that of the BL code(16) except at the stagnation point. The outflow boundary $\xi = 98°$ is obtained by means of two-point extrapolation. No adverse upstream influence is noticed since the flow no longer moves as fast as that on the spherical nose.

The preceding examples were obtained with $d_{e,2} = 0$ and $d_{e,4} \neq 0$. If $d_{e,2} > 0.0$, $\bar{S}_t$ and ε would have shown lower magnitude, but the calculation was stable without using $d_{e,2}$. For three-dimensional cases, however, $d_{e,2}$ is important in stabilizing the calculation. To examine its positive effects, the AEDC case was computed using three different $d_{e,2}$ values and the history of convergence is presented in Fig. 7. An inviscid calculation was obtained with $d_{e,2} = 0.1$ from $k = 0$ to 200, then the viscous calculation proceeded at different $d_{e,2}$ values. The influence of $d_{e,2}$ to the stability is self-explanatory. Nevertheless, the explicit damping is incapable of removing the spurious oscillations along a coordinate line. For instance, the C_H distributions were noted to swing up and down during the calculation with $CN = 50$ but to be smooth with $CN = 30$. The results at $k = 600$ (including 200 steps for inviscid calculation) are plotted in Fig. 8, but not shown is that the shock standoff distance near $\theta = 10°$ also oscillates with $CN = 50$. The value of C_H depends on the temperature gradient at the wall and thus is directly proportional to the shock-layer thickness at that point. Therefore, the accuracy of the viscous parameter, being very sensitive to the inviscid layer and shock calculations, should be used to evaluate the quality of the overall solutions. In contrast, the wall pressure distribution is relatively insensitive to shock shape and diffusive fluxes and cannot be used for that purpose.

The NSWC case 2 (Figs. 9 and 10) was considered to certify the conventional approach of finding starting data for aft-body calculation at $\alpha > 0°$. Since the flowfield over a sphere-cone is symmetric to the wind axis, an interpolation of the available 2D axisymmetric results will provide data on an axial plane for 3D cases. By selecting $Z_o = -0.5$, the outflow line at $\xi = \pi/2$ is quite close to the sonic line on the windward plane and, thus, may present upstream propagation of extrapolation error at the downstream boundary. The one-point extrapolation is deemed more stable than the two-point extrapolation that is used for the supersonic region. The pressure values are different at the stagnation point between the inviscid and viscous calculations. In Fig. 10, the heat-transfer distribution exhibits a small oscillation caused by the shock locations. More oscillations appeared in C_H and S_t when a grid of 28 by 12 by 3 was used instead of 33 by 12 by 3. Five additional grid points between the shock layer had resulted in more accurate shock fitting. Favorable comparison of the axial-plane data is found for 2D and 3D calculations at $\alpha = 10°$.

The AEDC case (Figs. 11 and 12) refers to the test environment of tunnel B, which was used extensively to develop an aerodynamic data base for the Space Shuttle Orbiter. For a simple hemispherical cone, the axial plane was placed at $Z_o = 0.5$ to minimize the upstream influence within the boundary layer. The Reynolds number is not high, and the wall temperature is about half the total temperature; hence, a grid of 28 by 12 by 5 is adequate to fit the shock and to resolve the crossflow gradient. In Fig. 12, a mild hump is displayed on the C_H distribution that can be attributed to the shock shape near $\xi = 0$. A few more grid points in η may smooth out both. The inviscid and viscous results are otherwise considered excellent. The data generated on the axial plane at $Z_o = 0.5$ were used to initialize both the Euler and the parabolized NS computation by the author(9) to an axial station equal to $Z_o = 30$.

The geometry of the Space Shuttle Orbiter was defined by a lofting technique using blueprint configuration. The Orbiter nose consists of a spherical cap at the nosetip and nonanalytical shape. The nonspherical configuration and $\alpha \geq 40°$ necessitate 3D NS calculations not only to determine C_H values but to find initial data for parabolized NS calculations. Under equilibrium-air assumption, the subsonic zone is well within the domain located at $Z_o = 0.5$. Using a grid of 8 by 16 by 8 and after 300 steps, the inviscid results have $\bar{S}_t = 2.9$ and $\varepsilon = 0.009$. The viscous calculations continued with a grid of 28 by 16 by 8 and another 300 steps of integration. The results have $\bar{S}_t = 0.4$ and $C_H = 0.04$. The Mach contours of the shock-layer flow are shown in Fig. 13. There are marked differences between inviscid and viscous results which may be attributed to the vortical flow enhanced by the presence of a viscous layer on the leeward side of the body. Another interesting pattern is that the locations of maximum p and maximum C_H are not necessarily at the same point on the body. (See Fig. 13.)

The grid points used to approximate the body and the shock are illustrated by Fig. 14 in two perspective views. They are very coarse for the size of the shock layer. The normalized data for the fifth Space Transportation System flight (STS-

5) are also presented. The discrepancy between the NS prediction and the data was also noted between the BL results and the data. No pressure data are available for comparison; however, the viscous pressure is somewhat higher than inviscid pressure on the windward side.

The aerobraking orbital transfer vehicle (AOTV) configuration represents the front portion of an ellipsoid/60° cone proposed by the NASA Lyndon B. Johnson Space Center for a flight experiment. The complete body consists of the front portion, a toroidal shoulder on a 15° raked plane, and a payload or propulsion bay. In the flowfield computation, the toroidal shoulder is replaced by a circular shoulder to facilitate computation. The shock and body grid network is shown in Fig. 15, together with the shock layer on the pitch plane. The purpose of Fig. 16 is to point out that the heat flux to the front surface is strongly affected by the discontinuities in body curvature, whereas the pressure is much less sensitive. The substantial differences between the inviscid and viscous pressure distributions (Fig. 16) imply that at such high altitudes, the viscous effects to the aerodynamic characteristics of the vehicle cannot be ignored. The computation time is 256 minutes, which accounts for both 200 and 300 iterations, respectively, for inviscid and viscous grids.

Concluding Remarks

Since the reports published in 1974 and 1975 of the Navier-Stokes solutions for asymmetric entry flow over blunt bodies, significant improvements have been made to the original 3D NS code. Although the formulation is still cast in curvilinear-orthogonal coordinates and uses a special equation to solve for the singular axis, the explicit scheme has been replaced by an ADI factorization technique combined with numerical damping and local-time increment. The code has a reliable and cost-saving procedure stepping from coarse to fine grids for solving viscous flow. Not only has the computational effort been reduced by a factor of 100 or more, the solution accuracy is also improved because of better understanding of the methodology. This code has a formulation, a numerical method, and an algebraic grid that are consistent to the level of accuracy desired for evaluating engineering design of space vehicles experiencing peak heating at high altitudes. We have finally succeeded in the stratagem by first developing an accurate formulation and then continuously improving the computational efficiency as better methods become available.

References

1. Hayes, W. D. and Probstein, R. F., *Hypersonic Flow Theory, Vol. 1, Inviscid Flows*, 2nd ed., Academic Press, New York, 1966.
2. Moretti, G. and Bleich, G., "Three-Dimensional Flow Around Blunt Bodies," *AIAA Journal*, Vol. 5, No. 10, 1967, pp. 1557-1562.
3. Rizzi, A. W. and Inouye, M., "Time-Split Finite-Volume Method for Three-Dimensional Blunt-Body Flow," *AIAA Journal*, Vol. 11, No. 11, 1973, pp. 1478-1485.
4. Hall, D. W., "Calculation of Inviscid Supersonic Flow over Ablated Nosetips," AIAA Paper 79-0342, *Aerospace Sciences Meeting*, New Orleans, La., Jan. 15-17, 1979.
5. Daywitt, J., "Improvements in Techniques for Computing Supersonic Blunt-Body Flows," AIAA Paper 81-0115, *19th Aerospace Sciences Meeting*, St. Louis, Mo., Jan. 12-15, 1981.
6. Li, C. P., "A Numerical Study of Laminar Flow Separation on Blunt Flared Cones at Angles of Attack," AIAA Paper 74-585, *7th Fluid and Plasma Dynamics Conference*, Palo Alto, Calif., June 17-19, 1974.
7. Goodrich, W. D. et al., "Scaling of Orbiter Aerothermodynamic Data Through Numerical Flow Field Simulations," NASA SP-347, Mar. 1975, pp. 1395-1410.
8. Beam, R. and Warming, R. F., "An Implicit Factored Scheme for the Compressible Navier-Stokes Equations," *AIAA Journal*, Vol. 16, Apr. 1978, pp. 393-401.
9. Li, C. P., "Numerical Simulation of Reentry Flow Around the Shuttle Orbiter Including Real Gas Effects," in *Computers in Flow Predictions and Fluid Dynamics Experiments*, Ed. by K. N. Ghia, T. J. Mueller, and B. R. Patel, ASME, 1981.
10. Kutler, P. et al., "Supersonic Flow Over Three-Dimensional Ablated Nosetips Using an Implicit Numerical Procedure," AIAA Paper 80-63, *18th Aerospace Sciences Meeting*, Pasadena, Calif., 1980.
11. Pulliam, T. H. and Steger, J. L., "On Implicit Finite-Difference Simulations of Three Dimensional Flow," AIAA Paper 78-10, *16th Aerospace Sciences Meeting*, Huntsville, Ala., Jan. 16-18, 1978.
12. Tannehill, J. V. and Mugge, P. H., "Improved Curve Fits for the Thermodynamic Properties of Equilibrium Air Suitable for Numerical Computation Using Time-Dependent or Shock-Capturing Method," Iowa State University Rept. ISU-ERI-Ames-74050, Feb. 1974.
13. Vigneron, Y. C., "Hypersonic Viscous Flow of Equilibrium Air Around a Blunt Body," M.S. Thesis, Iowa State University, 1976.
14. Tannehill, J. V. et al., "Numerical Computation of Two-Dimensional Viscous Blunt Body Flows with an Impinging Shock," *AIAA Journal*, Vol. 4, Feb. 1976.
15. Hsieh, T. Y., "Calculation of Viscous Hypersonic Flow over a Severely Indented Nosetip," *AIAA Journal*, Vol. 22, No. 7, July 1984, pp. 935-941.
16. Tong, H. et al., "Nonequilibrium Chemistry Boundary Layer Integral Matrix Procedure," Aerotherm Rept. 73-67, NAS 9-9494, July 1973.

Appendix A - Derivation of Eq. (2)

Equation (1) is undeterminate or singular along the Z-axis because of $\sin \xi = 0$ and $w = 0$. In the removal of $\sin \xi$ or ξ from the flux terms, $\bar{h}_{\zeta\xi}$ has a complicated expression and needs special analysis. Consider a typical component of $\bar{h}$; the mixed derivative of second order results in

$$(\rho w)_{\zeta\xi} = \rho_{\zeta\xi} w + \rho_\xi w_\zeta + \rho_\zeta w_\xi + \rho w_{\zeta\xi} \qquad \text{(A1)}$$

But the velocity components are related on the Z-axis by

$$u = u(0, \eta, 0) \cos \zeta, v = v(0, \eta, 0), w = -u(0, \eta, 0) \sin \zeta$$

Hence, when evaluating Eq. (A1) on the pitch plane $\zeta = 0$, one observes that

$$w = 0,\ w_\zeta = -u(0,\eta,0),\ w_\xi = 0,\ w_{\zeta\xi} = -u_\xi(0,\eta,0)$$

and $$(\rho w)_{\zeta\xi} = -\rho_\xi u(0,\eta,0) - \rho u_\xi(0,\eta,0) \neq -(\rho u^*)_\xi$$

where $u^* = u(0,\eta,0)$. Thus, the convective $\bar{h}$ flux becomes

$$\bar{h}_{\zeta\xi} = -\frac{u(0,\eta,0)}{u} \bar{f}_\xi - u_\xi(0,\eta,0)\, \bar{u}$$

and $$\bar{f} = \begin{bmatrix} \rho u \\ \rho u^2 \\ \rho u v \\ 0 \\ \rho u \varepsilon + p u \end{bmatrix}, \quad \bar{u} = \begin{bmatrix} \rho \\ \rho u \\ \rho v \\ 0 \\ \rho \varepsilon + p \end{bmatrix}$$

since

$$(\ )_\xi = (\ )_x + y_\xi(\ )_y,\ (\ )_\zeta = (\ )_z + y_\zeta(\ )_y, \text{ and}$$

$$(\ )_\eta = (\ )_y$$

The final form is

$$\bar{h}_{\zeta\xi} = -\frac{u^*}{u}\left(\bar{f}_x + y_\xi \bar{f}_y\right) - \left(u_x + y_\xi u_y{}^*\right) \bar{u}$$

This term, in conjunction with $(\bar{f} + \bar{r})/\sin \xi$ from Eq. (1), completes the derivation of the convective portion of Eq. (2).

An evaluation of the diffusive fluxes on the Z-axis is not pursued analytically; instead, an approximated expression is derived using difference formula and grid notation presented in sec. 3.1. Let H be the diffusive fluxes. Then

$$H_{\xi\zeta} = H_{zx} + y_\xi H_{zy}$$

where

$$H_{zx} = \left[\left(H_{n,3,3} + H_{n,1,1}\right)/\left(2\,\Delta z\right) - \left(H_{n,3,1} + H_{n,1,3}\right)/\left(2\,\Delta z\right)\right]/\left(2\,\Delta x\right)$$

$$H_{zy} = \left[\left(H_{n+1,2,3} + H_{n-1,2,1}\right)/\left(2\,\Delta z\right) - \left(H_{n+1,2,1} + H_{n-1,2,3}\right)/\left(2\,\Delta z\right)\right]/\left(2\,\Delta y\right)$$

Table 1 Unit vectors in reference coordinate frames

	Wind frame $\bar{I}, \bar{J}, \bar{K}$	Cartesian frame I, J, K	Spherical frame i, j, k
Cartesian frame $I, J, K =$	$\bar{I}\cos\alpha + \bar{K}\sin\alpha$	1	$i\cos\xi\cos\zeta + j\sin\xi\cos\zeta - k\sin\zeta$
	$\bar{J}$	1	$i\cos\xi\sin\zeta + j\sin\xi\sin\zeta + k\cos\zeta$
	$-\bar{I}\sin\alpha + \bar{K}\cos\alpha$	1	$i\sin\xi - j\cos\xi$
Spherical frame $i, j, k =$		$I\cos\xi\cos\zeta + J\cos\xi\sin\zeta + K\sin\xi$	1
		$I\sin\xi\cos\zeta + J\sin\xi\sin\zeta - K\cos\xi$	1
		$-I\sin\zeta + J\cos\zeta$	1
Intrinsic frame $n, t, b =$			$i n_1 + j n_2 + k n_3$
			$i t_1 + j t_2$
			$i b_1 + j b_2 + k b_3$

e.g., $\vec{V} = iu + jv + kw = IU + JV + KW, \quad U = I \cdot V = I \cdot iu + I \cdot jv + I \cdot kw$

Table 2 List of sample cases

Case	M	α, deg	α_T, deg	Z_o[a]	Grid	Model[b]	T_w	Re[c]	R_N,[d] ft
NSWC-1	2.97	0	0	0	8 by 12	P	1	1.01×10^6	0.1823
	5.94				28 by 12				
NSWC-2	5.94	10	0	-0.5	8 by 12 by 3	P	4.4	1.01×10^6	0.1823
					33 by 12 by 3				
AEDC	8	30	0	0.5	8 by 12 by 5	P	6.5	0.71×10^6	0.0413
					28 by 12 by 5				
Orbiter	22	40.8	0	0.5	8 by 16 by 8	E	8.5	14 000	2.36
					28 by 16 by 8				
AOTV	34.8	0	15	NA	10 by 18 by 5	P	8.4	8272	10
					28 by 18 by 5				

[a] Location of the Cartesian frame relative to the center of the nose curvature on Z-axis.

[b] P–perfect gas ($\gamma = 1.4$), E – equilibrium air.

[c] Free-stream Reynolds number per foot.

[d] Nose radius on Z-axis.

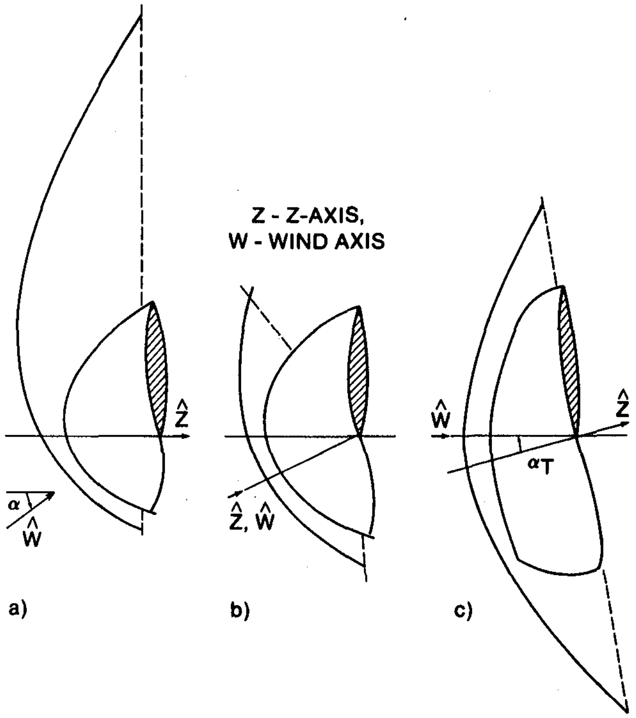
Z - Z-AXIS,
W - WIND AXIS
$\hat{Z}$
α
$\hat{W}$
a)
$\hat{Z}, \hat{W}$
b)
$\hat{W}$
$\hat{Z}$
α_T
c)

Fig. 1 Capabilities of the Navier-Stokes/Euler blunt-body code. a) Portion of a complete Orbiter flowfield. b) Stagnation region of blunt body. c) OTV with raked-off body.

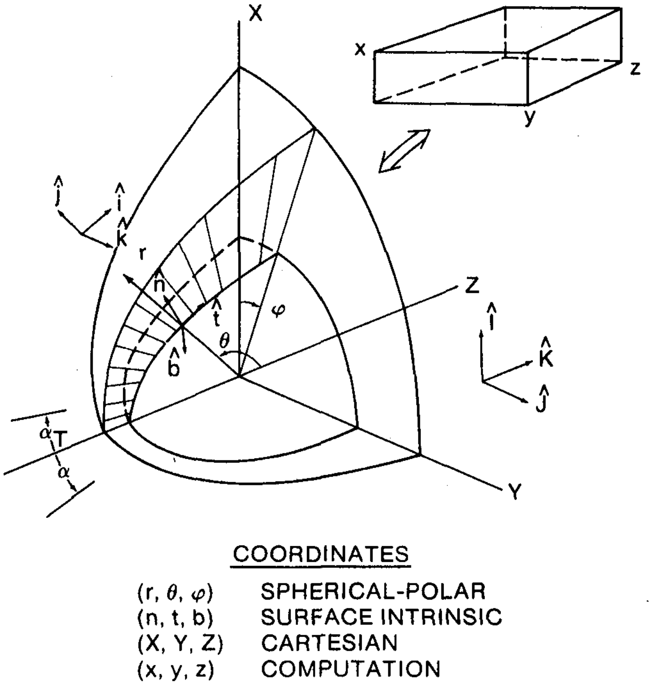
X
x
z
y
$\hat{j}$
$\hat{i}$
$\hat{k}$
r
$\hat{n}$
$\hat{t}$
$\hat{b}$
θ
φ
Z
$\hat{I}$
$\hat{K}$
$\hat{J}$
α_T
α
Y
COORDINATES
(r, θ, φ) SPHERICAL-POLAR
(n, t, b) SURFACE INTRINSIC
(X, Y, Z) CARTESIAN
(x, y, z) COMPUTATION

Fig. 2 Schematic of the physical and computational coordinates.

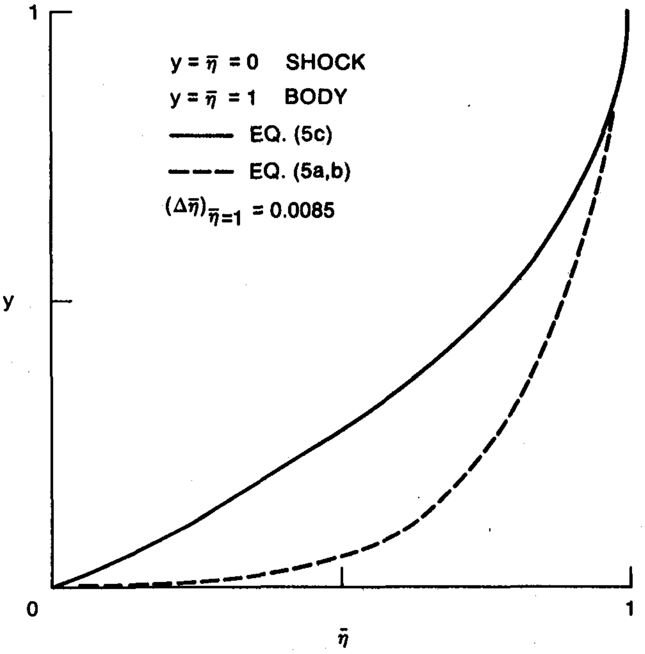

Fig. 3 Comparison of the grid-clustering functions.

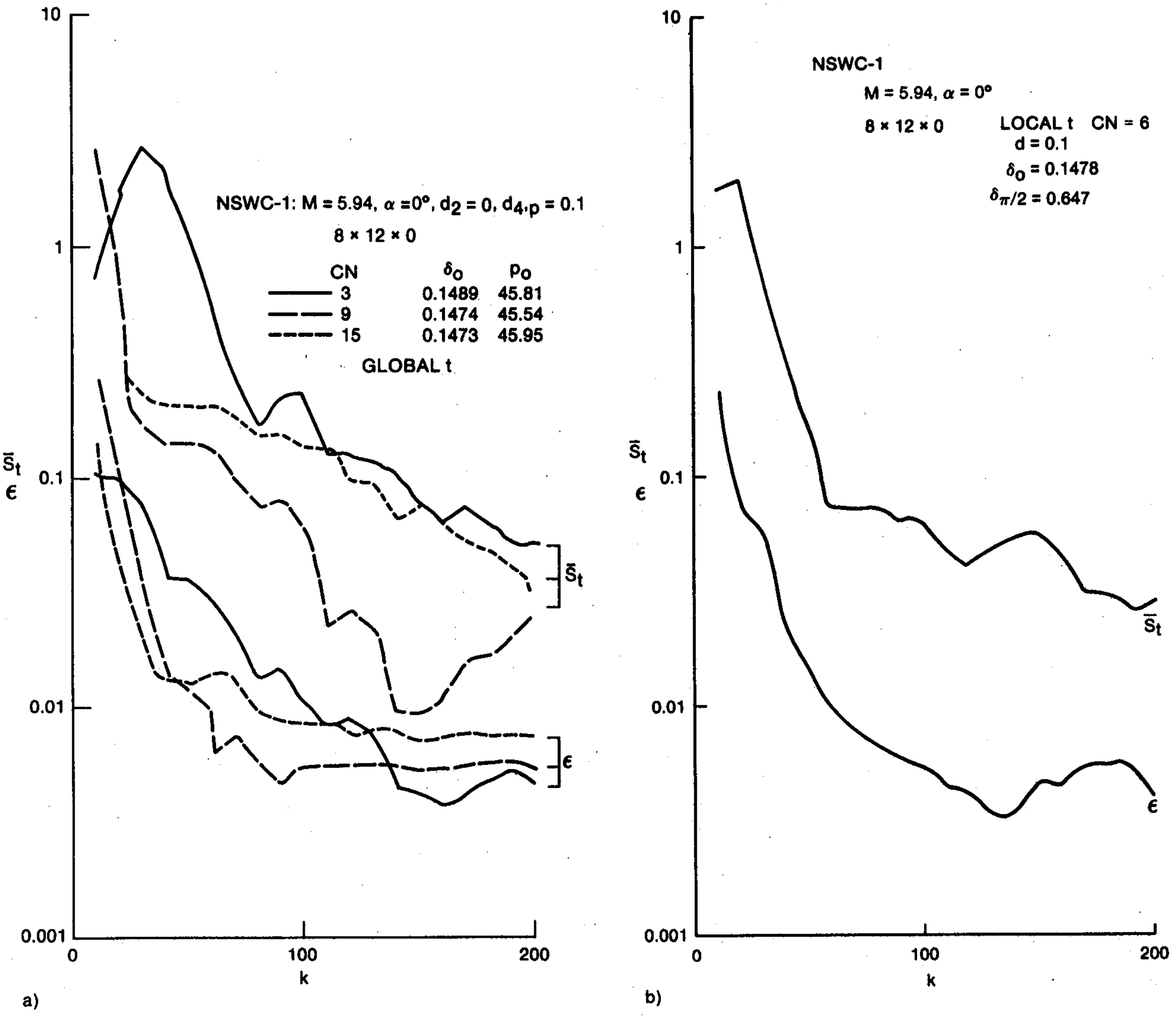

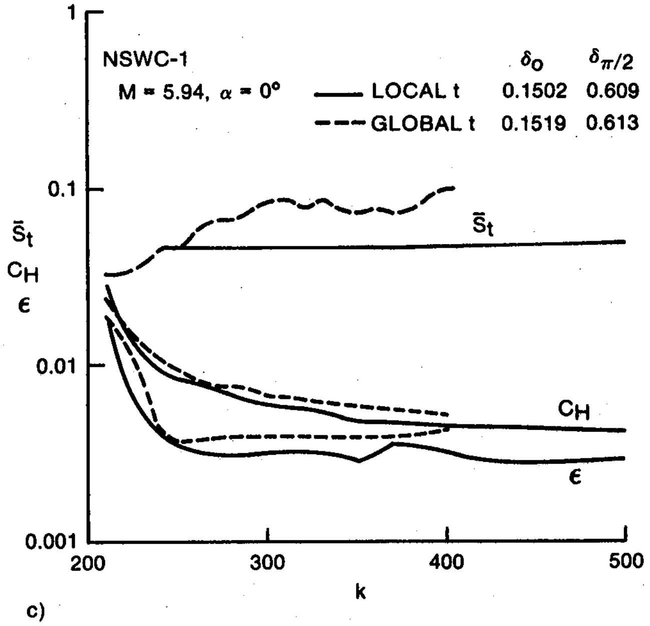

Fig. 4 Convergence history for 2D NSWC-1 case. a) Effects of time-increment step size on inviscid solution. b) Effects of local-time integration on inviscid solution. c) Comparison between global- and local-time convergence rates for viscous case.

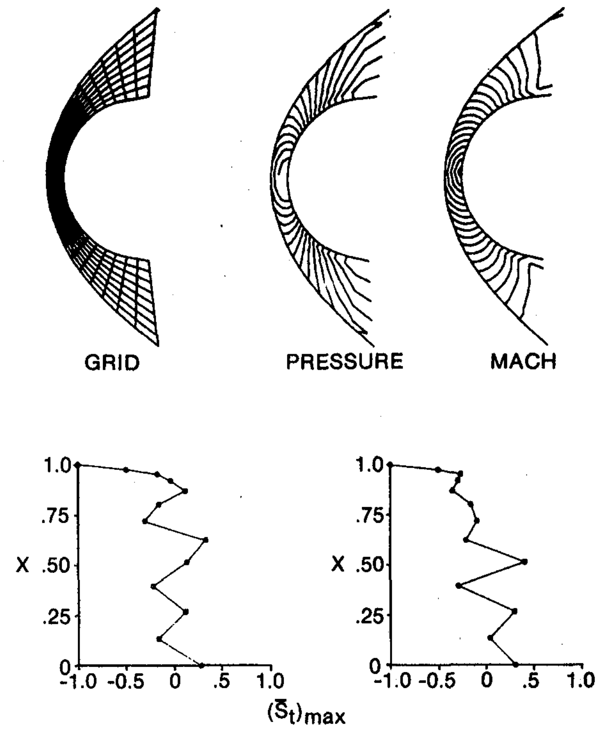

Fig. 5 Inviscid flowfield results for the NSWC-1 case (M = 2.97, α = 0°); X_{max} = 0.58102. Shock speed: 0.003187 (left plot); 0.005339 (right plot).

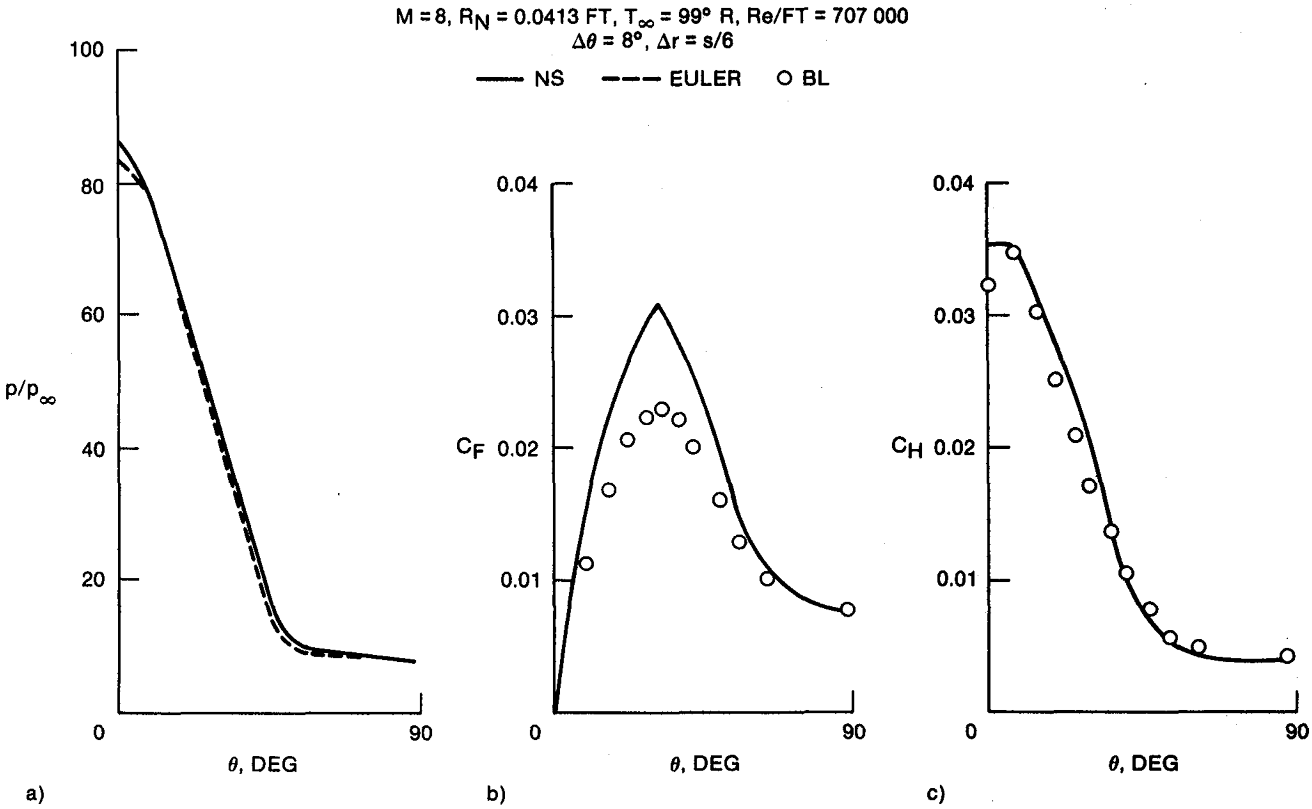

Fig. 6 Comparison of NS and BL results for an AEDC 2D case. a) Wall pressure distribution. b) Friction coefficient. c) Heat-transfer coefficient.

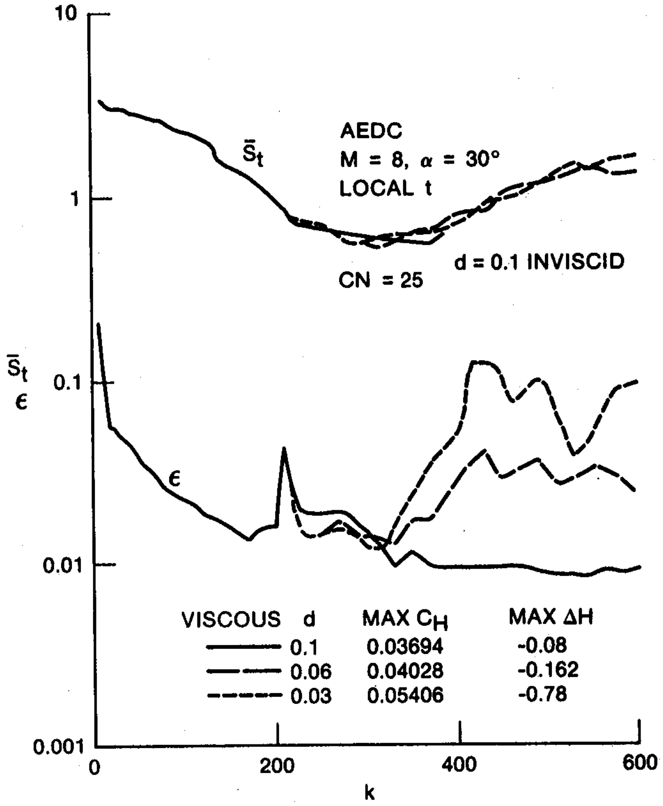

Fig. 7 Convergence history for an AEDC 3D case and effects of damping parameters.

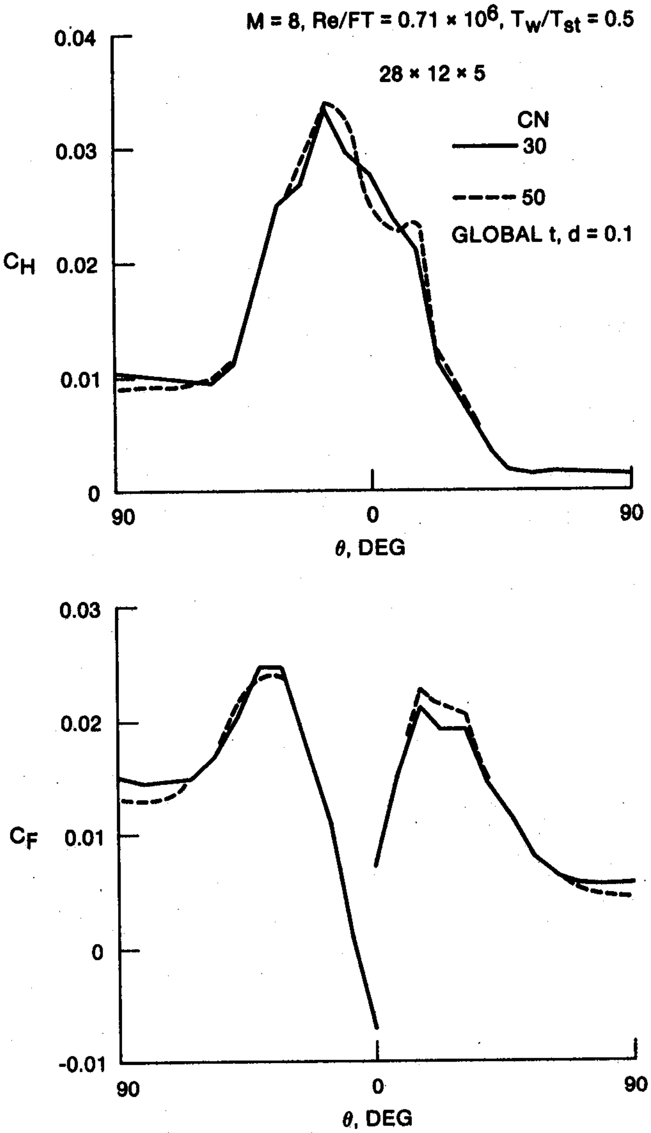

Fig. 8 Comparison of friction and heat-transfer coefficients for an AEDC 3D case using different time-step sizes.

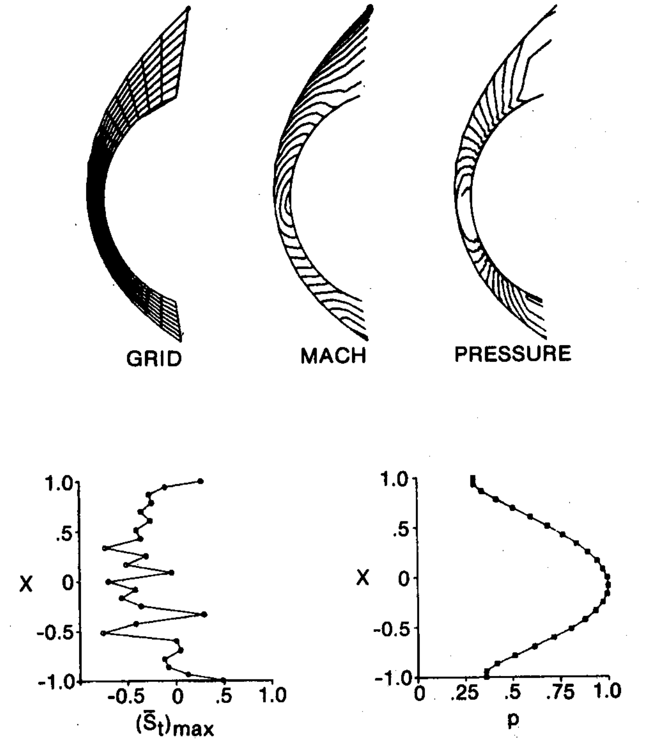

Fig. 9 Inviscid flowfield results for the NSWC-2 case (M = 5.94, α = 10°); X_{max} = 0.9496. Shock speed, 0.017368 (left plot); stagnation pressure, 44.5016 (right plot).

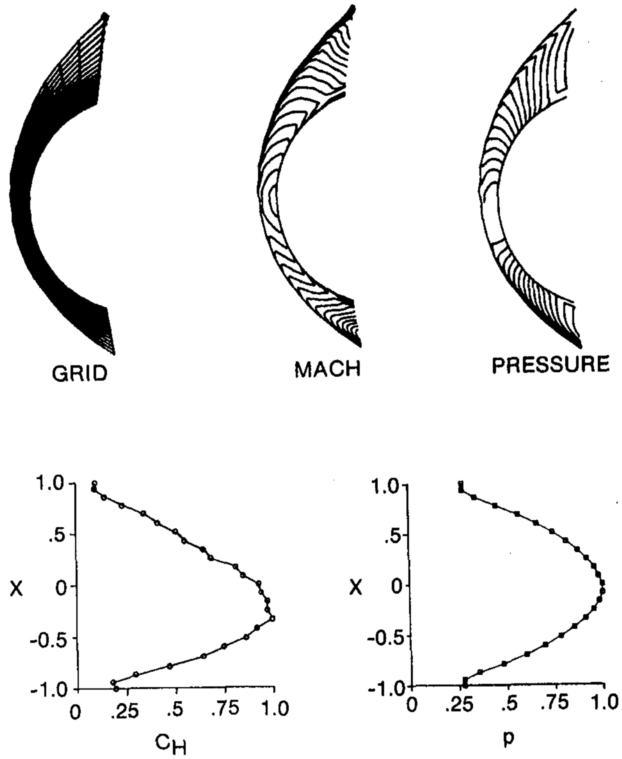

Fig. 10 Viscous flowfield results for the NSWC-2 case (M = 5.94, α = 10°); X_{max} = 0.9496. Stagnation Stanton number, 0.00374 (left plot); stagnation pressure, 43.2118 (right plot).

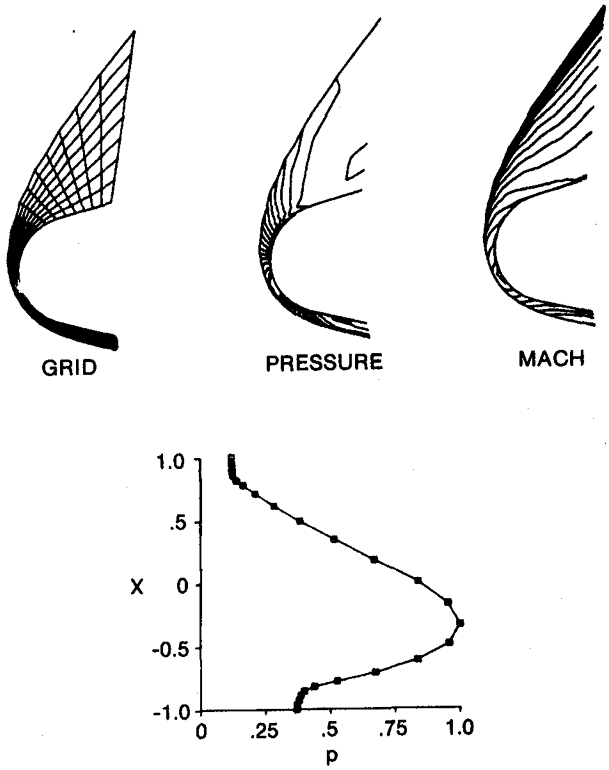

Fig. 11 Inviscid flowfield results for the AEDC case (M = 8, α = 30°). X_{max} = 1.2161; stagnation pressure, 77.2282.

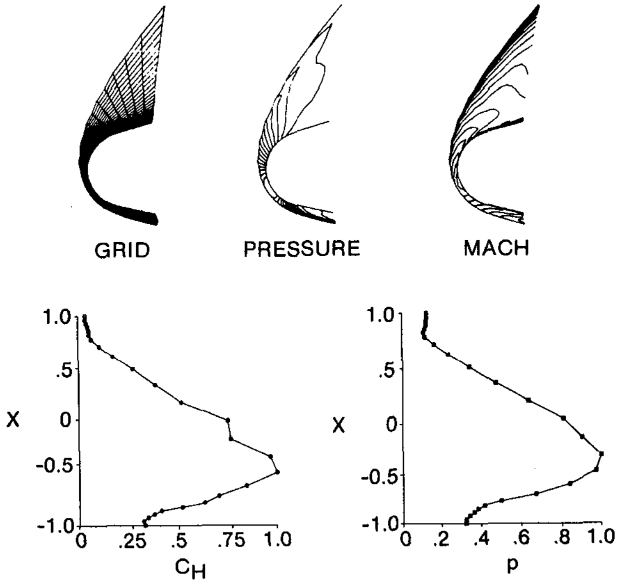

Fig. 12 Viscous flowfield results for the AEDC case (M = 8, α = 30°). X_{max} = 1.2161; stagnation pressure, 82.1822 (right plot); stagnation Stanton number, 0.03695 (left plot).

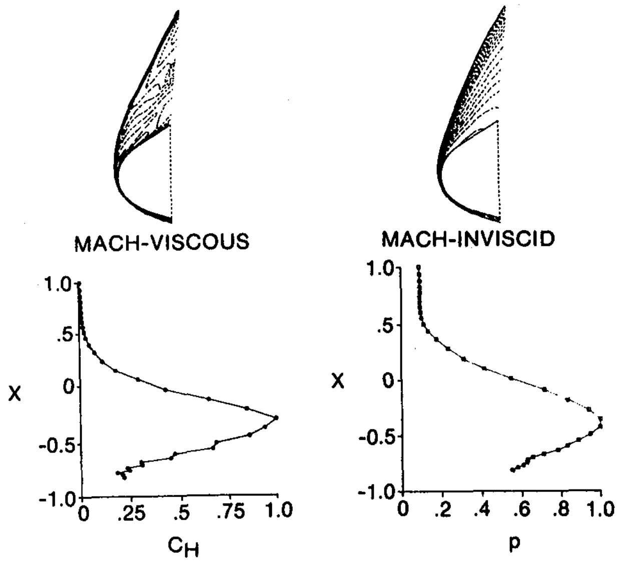

Fig. 13 Inviscid and viscous flowfield results for the Orbiter case (M = 22, α = 40.8°, equilibrium air); X_{max} = 1.613. Stagnation Stanton number, 0.03796 (left plot); stagnation pressure, 663.748 (right plot).

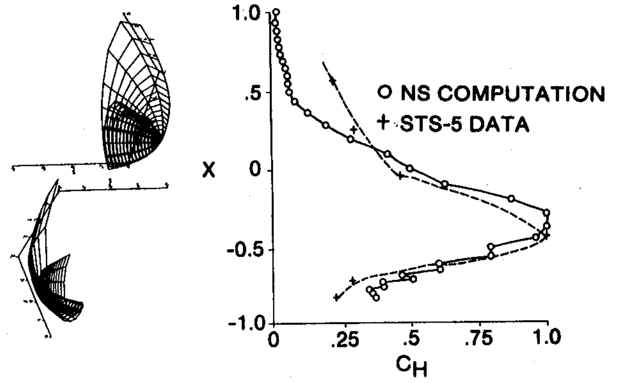

Fig. 14 Shock shape and comparison with flight data for the Orbiter case (α = 40.8°, t = 650 sec). X_{max} = 1.613; stagnation Stanton number, 0.040736.

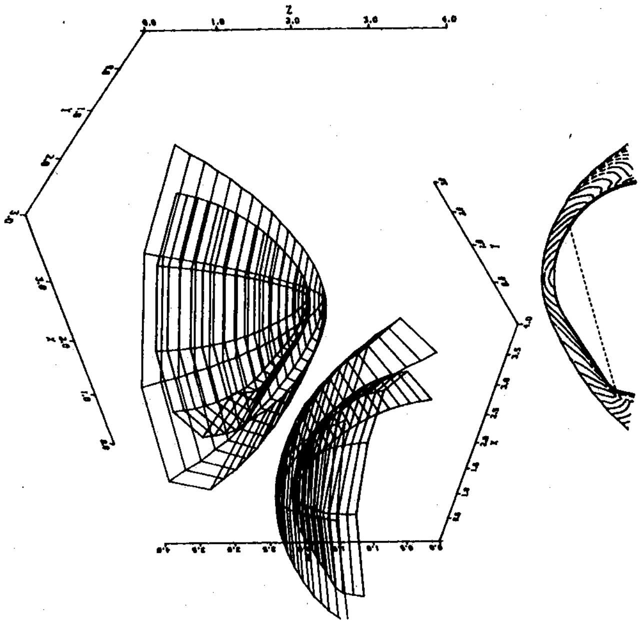

Fig. 15 Shock shape for the OTV case (M = 34.8, α_T = 15°).

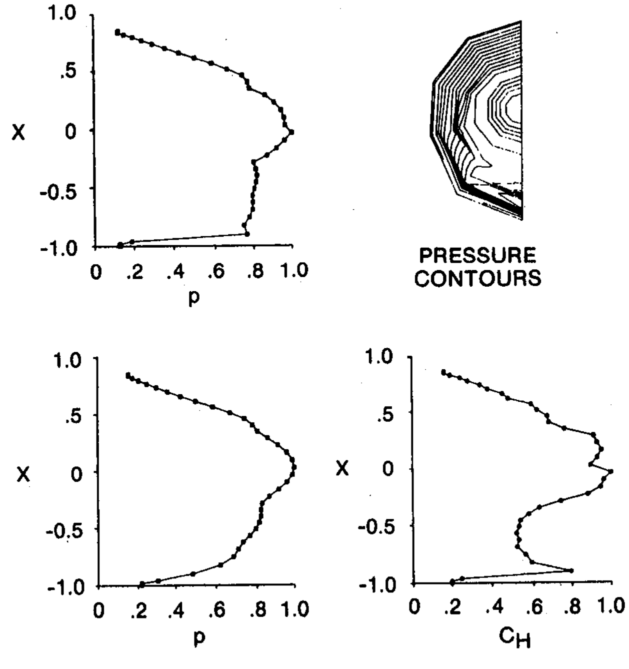

Fig. 16 Inviscid and viscous flowfield results for the OTV case; X_{max} = 2.493. Stagnation Stanton number, 0.02512 (lower right); stagnation pressure: 1540.56 (upper left); 1553.33 (lower left, viscous case).

1. Report No. NASA TM-58266	2. Government Accession No.	3. Recipient's Catalog No.

4. Title and Subtitle A THREE-DIMENSIONAL NAVIER-STOKES/EULER CODE FOR BLUNT-BODY FLOW COMPUTATIONS	5. Report Date April 1985 6. Performing Organization Code 506-51-17-00-72
7. Author(s) Chien-peng Li	8. Performing Organization Report No. S-546
9. Performing Organization Name and Address Lyndon B. Johnson Space Center Houston, Texas 77058	10. Work Unit No. 11. Contract or Grant No.
12. Sponsoring Agency Name and Address National Aeronautics and Space Administration Washington, D.C. 20546	13. Type of Report and Period Covered Technical Memorandum 14. Sponsoring Agency Code

15. Supplementary Notes

16. Abstract

The shock-layer flowfield is obtained with or without viscous and heat-conducting dissipations from the conservative laws of fluid dynamics equations using a shock-fitting implicit finite-difference technique. The governing equations are cast in curvilinear-orthogonal coordinates and transformed to the domain between the shock and the body. Another set of equations is used for the singular coordinate axis, which, together with a cone generator away from the stagnation point, encloses the computation domain. After initializing the flow variables on a prescribed grid, a time-dependent alternating direction implicit factorization technique is applied to integrate the equations with local-time increment until a steady solution is reached. The shock location is updated after the flowfield computation, but the wall conditions are implemented into the implicit procedure. Since primitive variables and few metrics are used, the numerical formulation is simple and the core requirement is not stringent. Innovative procedures have been introduced to define the initial flowfield, to treat both perfect and equilibrium gases, to advance the solution on a coarse-to-fine grid sequence, and to start viscous flow computations from their corresponding inviscid solutions. The code has proven capabilities for a wide range of free-stream conditions and body configurations. Among the examples shown are the Space Shuttle Orbiter equilibrium flow case at Mach 22 and an angle of attack of 40.8°, and an aerobraking orbital transfer vehicle perfect-gas case having a 60° cone and sonic shoulder at Mach 34.8. These results are obtained from a grid no greater than 28 by 18 by 7 and converged within 300 integration steps. They are of sufficient accuracy to start parabolized Navier-Stokes or Euler calculations beyond the nose region, to compare with flight and wind-tunnel data, and to evaluate conceptual designs of reentry spacecraft.

17. Key Words (Suggested by Author(s)) Hypersonic flowfield Computational fluid dynamics Numerical integration	18. Distribution Statement Unclassified - Unlimited Subject Category 02

19. Security Classif. (of this report) Unclassified	20. Security Classif. (of this page) Unclassified	21. No. of Pages 27	22. Price*

*For sale by the National Technical Information Service, Springfield, Virginia 22161